Multiple sclerosis iPSC derived-pericytes contract poorly but respond robustly to lesion-relevant environmental stimuli

Alastair J Fortune[1], Natalie E King[1], Ariane Gélinas-Marion[1], Roisin A Moloney[1], Jake M Cashion[2], Kathryn P Burdon[1], Bruce V Taylor[1], Brad A Sutherland[2], Jessica L Fletcher[1*], Nicholas B Blackburn[1*], Kaylene M Young[1*#]

Affiliations:

[1] Menzies Institute for Medical Research, University of Tasmania, 17 Liverpool St, Hobart, Australia, 7000

[2] Tasmanian School of Medicine, University of Tasmania, 17 Liverpool St, Hobart, Australia, 7000

* Authors contributed equally to this work

Corresponding author (kaylene.young@utas.edu.au)

Abstract:

Multiple sclerosis (MS) is associated with vascular abnormalities including blood-brain-barrier disruption, neurovascular uncoupling and cerebral hypoperfusion. As pericytes regulate vascular integrity and capillary diameter, pericyte dysfunction may contribute to MS pathophysiology. To investigate this, we generated induced pluripotent stem cell-derived pericytes (iPericytes) from individuals with or without relapsing-onset MS (RoMS). RoMS iPericytes exhibited intrinsic, cell-autonomous alterations in gene expression, were larger, and responded poorly to the vasoconstrictor, endothelin-1. Despite intrinsic differences, Control and RoMS iPericytes phagocytosed myelin debris and responded robustly to lesion-relevant stimuli. Hypoxia induced iPericyte proliferation, elongation and angiogenic and immune-related gene expression, while exposure to MS-relevant cytokines (TNFα and IFNγ) exacerbated the endothelin-1-evoked contraction. Both RoMS and cytokine exposure altered the expression of calcium and myosin signalling genes downstream of endothelin-1, including the key contractile regulator *MYLK*. These data support intrinsic pericyte dysfunction and signalling within MS-lesions as drivers of hypoperfusion and neurodegeneration in MS.

Keywords: pericytes, multiple sclerosis, contractility, cytokines, hypoxia, myelin, iPSC

Main

Multiple sclerosis (MS) is characterised by central nervous system (CNS) inflammation, demyelination and neuron death [1]. In addition to these hallmark pathologies, people with MS experience blood-brain-barrier (BBB) disruption [2-5], impaired neurovascular coupling (Marshall et al., 2016; Marshall et al., 2014), and cerebral hypoperfusion in the grey [6-10] and white matter [11-13]. Cerebral hypoperfusion likely drives the development of hypoxia in MS brain tissue [14-19], which would exacerbate neuroinflammation and neurodegeneration, and impede remyelination [20]. It remains unclear however, whether hypoperfusion is a primary pathology in people with MS. Over 200 MS susceptibility variants have been identified [21], and many of the genes linked to these variants are expressed by cells within the neurovascular unit, implicating vascular cells as contributing to disease risk [21,22]. These or other variants could intrinsically change the structure or function of key neurovascular cell types [23,24].

The neurovascular unit, composed of endothelial cells, astrocytes, neurons and pericytes, regulates BBB permeability, and modulates blood flow in response to the changing metabolic and oxygen demands of the CNS [25-27]. Throughout the brain capillary network, a single layer of endothelial cells forms the vessel walls and pericytes, embedded in the basement membrane, extend processes around the vessels that contract and relax to regulate vascular tone [25,28]. Pericytes can be identified by their expression of platelet-derived growth factor receptor β (PDGFRβ), the NG2 proteoglycan, CD13 and, specifically within the CNS, by ATP13A5 [29], and while PDGFRβ^{+} cells are present within MS lesions, the exact identity, functional state or contribution of these cells to MS pathophysiology has not been determined [27,30,31].

Pericytes perform a diverse range of roles that could enable them to play a primary and / or secondary role in MS pathophysiology [32,33]. For example, pericytes can produce inflammatory cytokines and enhance macrophage extravasation [30]. Interestingly, pericyte loss also promotes vascular and immune pathologies, with pericyte depletion being sufficient to reduce BBB integrity, upregulate the expression of leukocyte adhesion molecules on endothelial cells, and promote peripheral immune cell extravasation in the CNS [34-36]. While pericyte density is reduced in the cerebellum of mice with experimental autoimmune encephalomyelitis (EAE) [30], it is unclear if this pericyte loss drives the associated diminished cerebrovascular reactivity or increased leukocyte stalling and extravasation [37].

These mouse studies highlight the capacity for pericytes to contribute to MS pathophysiology. However, they cannot determine whether pericytes experience intrinsic dysfunction prior to MS onset, that could also modify their response to pathological signalling within MS lesions. These questions can be answered by differentiating induced pluripotent stem cells (iPSCs) from people with and without relapsing onset MS (RoMS) to obtain pericyte-like cells (iPericytes; [23,38,39] for direct interrogation.

Herein, we report that the expression of contractility-related genes is altered in RoMS iPericytes, and that their contractile response to endothelin-1 (ET-1) is impaired. This intrinsic pericyte dysfunction would compromise capillary blood flow regulation and

contribute to cerebral hypoperfusion. We also report that pericyte function is modulated by MS lesion-associated stimuli including exposure to myelin debris, hypoxia, and inflammatory cytokines. Notably, pre-exposure to TNFα and IFNγ drives an excessive contractile response to ET-1 that would be predicted to significantly reduce capillary blood flow within lesions. These findings position pericytes as active contributors to MS pathogenesis and progression, and a potential therapeutic target for neuroprotection in MS.

Results

Transcriptomic profiling reveals intrinsic alterations in contractile and vascular regulatory pathways in RoMS iPericytes

To determine whether pericytes are intrinsically altered in people with MS, we obtained blood from people without MS (n=10, Controls), MS-affected members of a multi-case family (n=4, Family RoMS cases spanning 2 generations) or unrelated people with RoMS (n=8, RoMS cases). Peripheral blood mononuclear cells were isolated and used for Sendai-virus mediated iPSC generation as previously described [40,41]. The resulting 22 iPSC lines (**Table 1**) were differentiated into iPericytes using a validated protocol [38,39] (**Fig. 1a**), and immunocytochemistry performed to confirm that > 95% of the cells in each culture expressed the pericyte proteins PDGFRβ and CD13 (*ANPEP*) (**Fig. 1b**; **Fig. S1a**). RNA was subsequently isolated from iPericytes and bulk RNA sequencing performed to confirm successful differentiation. iPericytes exhibited a transcriptional profile consistent with human brain vascular pericytes, with a high level of expression of pericyte genes and minimal expression of genes specific to other CNS-resident cell types (**Fig. S1b**). Of the 551 genes potentially impacted by MS-associated risk variants [22], 427 were expressed by iPericytes, with 142 being upregulated during iPericyte differentiation (**Fig. S1c**). These data indicate that any dysregulation of these genes that increases MS risk could be impacting pericyte function.

To determine whether RoMS iPericytes have transcriptional signatures distinct from Controls, we compared the transcriptome of Control, Family RoMS, and RoMS iPericytes. Global gene expression analysis using PCA revealed partial separation along PC2 (9% of variance) of Control, Family RoMS, and RoMS samples (**Fig. 1c**). Our initial differential gene expression analysis compared Control and Family RoMS iPericytes ($\log_2$FC>0.1, α<0.05) and identified 251 differentially expressed genes (DEGs) (**Fig. 1d**), including regulators of cell contraction, such as decreased expression of *myosin light chain 12A (MYL12A;* LFC=0.3, Padj=0.048) and *calcium-activated potassium channel subunit α1* (*KCNMA1*; LFC=-1.7, Padj=0.003) (**Data TS1**) [42,43]. Gene set enrichment analysis revealed that vascular smooth muscle contraction and microtubule organisation pathways were suppressed (**Fig. 1e, Data TS2**), suggesting that contractility may be disturbed in Family RoMS iPericytes. As alternative splicing of genes can impact elements of the contractile machinery in pericytes [44], we also performed differential transcript usage (DTU) analysis. Comparing Control and Family RoMS iPericytes we identified 18 genes with DTU (**Fig. S1d, Data TS3**), including *RND3* (a gene associated with an MS risk variant [21]), which

encodes a Rho GTPase that can regulate contractility and blood flow [45,46]. In Family RoMS iPericytes, we also found that the *CDKN2A* isoform encoding the p16^{INK4A} cellular senescence protein was upregulated (**Fig. S1e**). As p16^{INK4A} expression is upregulated in neural progenitor cells in primary progressive MS postmortem brain tissue and in iPSC-derived neural progenitor cells from progressive MS donors [47,48], this may represent a common phenotype across cell types.

Our comparison of Control and RoMS iPericyte samples identified only 3 differentially expressed genes (**Fig. 1f, Data TS4**). RoMS iPericytes having fewer significant transcriptional changes than Family RoMS iPericytes would be consistent with the cause and level of intrinsic dysfunction being more varied in unrelated MS cases. However, there were also 11 genes with significant DTU (**Fig. S1f, Data TS5**). This included alternative splicing of *myosin light chain kinase* (*MYLK;* Padj=0.015), which was driven by the decreased expression of the canonical *MYLK* transcript (**Fig. 1g, Fig. S1g**), which encodes the calcium-dependent myosin light chain kinase (MLCK). Pericyte contractile state is strongly influenced by the activity of MLCK, which phosphorylates the myosin light chains to drive contraction [26], and works in concert with the myosin light chain phosphatase (MLCP), which promotes relaxation (Wilhelm et al., 2025). Interestingly, Family RoMS exhibited increased expression of the shortest characterised isoform of *MYLK*, which encodes the protein Telokin (**Fig. 1g**). Telokin inhibits MLCK-mediated phosphorylation of myosin light chains, while enhancing MLCP activity, thereby desensitizing cells to calcium-mediated contractility [49,50]. Therefore, while mediated by distinct isoform changes in Family RoMS and RoMS iPericytes, both gene expression changes would diminish MLCK activity and be predicted to reduce pericyte contractility.

To gain further insight into key dysregulated pathways, we compared Control samples with All RoMS (n=12, Family RoMS+RoMS) and identified 18 DEGs (**Fig. 1h, Data TS6**). Downregulated genes included components of the myosin light (*MYL11*) and heavy chains (*MYH3*, *MYH7*) (**Fig. 1i**), and enrichment analysis confirmed that pathways associated with contraction, blood circulation, and vascular development were significantly altered (**Fig. 1j, Data TS7**). These data indicate that Family RoMS and RoMS iPericytes have intrinsic transcriptional changes that are likely to impact actomyosin-mediated contraction.

RoMS iPericytes are enlarged and contract poorly following endothelin-1 exposure.

To determine whether intrinsic changes in RoMS iPericyte gene expression altered iPericyte structure or function, we collected phase contrast images of Control, Family RoMS and RoMS iPericyte cultures and performed a morphological analysis. Across all groups, individual cells adopted a mixture of pericyte standard, spindle, sheet or circular morphologies [39,51] (**Fig. S2a**). Standard morphology predominated, and the overall distribution of morphologies was comparable between Control and Family RoMS cultures (**Fig. S2a**). Consistent with this, iPericyte elongation, indicated by maximum Feret diameter (diameter at widest point / perimeter length), was unaffected by MS status (**Fig. S2b**). However, by tracing the perimeter of individual pericytes in each culture (**Fig. 2a**), and quantifying cell area and perimeter length, we determined

that Family RoMS and RoMS iPericytes were significantly larger than Control iPericytes (**Fig. 2b,c**). This may be directly due to changes to myosin subunits [51,52], but could also be impacted by a change in proliferation kinetics. To evaluate this possibility, Control, Family RoMS and RoMS iPericytes were exposed to the thymidine analogue, ethynyl-2'-deoxyuridine (EdU) for 20 hours. EdU^+ pericytes were detected in all cultures (**Fig. S2c**), but the proportion of iPericyte that had undergone division and incorporated EdU was unaffected by MS status (**Fig. S2d**). The increased cell size was also unrelated to a change in basal motility (**Fig. S2e-g**) but could reflect a change in contractile state.

To determine whether RoMS iPericyte contractility was altered, we exposed Control Family RoMS and RoMS iPericytes to endothelin-1 (ET-1). ET-1 is a potent pericyte vasoconstrictor [39,53,54] (**Fig. S2h, i**), and iPericytes from all groups express the *EDNRA* transcript, which encodes the primary ET-1 receptor (LFC=-0.00002, padj=0.999; **Fig. S2j**). Following ET-1 application, we quantified the size of the evoked contraction by measuring electrical impedance: when iPericytes contract they reduce their surface area, reducing electrical impedance (cell index) across the plate (**Fig. 2d**). We found that iPericytes from Control, Family RoMS, and RoMS participants had similar contraction kinetics, reaching their maximal contraction after ~14 minutes. However, the magnitude of contraction differed significantly between groups. The contractile response was significantly impaired in Family RoMS and RoMS iPericyte, with the evoked contractions reaching 64.1% and 78.3% of the maximal Control contraction, respectively (**Fig. 2e**). Furthermore, the volume of contraction, given by the area under the curve (AUC), was markedly decreased in Family RoMS and RoMS iPericytes (**Fig. 2f**). These data demonstrate that the intrinsic gene expression changes within contractile signalling pathways manifests as significantly impaired contraction by Family RoMS and RoMS iPericytes.

As pericytes modulate blood flow through vasoconstriction and vasodilation [25,39], we next evaluated the capacity of iPericytes to relax when exposed to the vasodilator, adenosine [39,51]. iPericyte cultures contracted when the E-plate was removed from the incubator but relaxed significantly following the addition of 10μM adenosine (**Fig. 2g**). We found that Family RoMS iPericytes had equivalent maximum and volume of Control iPericytes, indicating a preserved ability to relax (**Fig. 2h,i**). Pericytes exist in a partially constricted state at rest to provide basal tone for capillaries, but dynamically respond to vasoconstrictors and vasodilators to direct blood flow to metabolically active regions [25,26]. Within the CNS, a local reduction in pericyte contraction in response to ET-1 would increase blood flow through the capillary bed, however, as we predict this would instead impact tone across the entire RoMS brain capillary network, it would be more likely to increase capillary blood volume but reduce flow rate, leading to hypoperfusion (**Fig. S3a**). Consistent with this hypothesis, hypoperfusion is a feature of clinically isolated syndrome [55], a clinical presentation that can precede an MS diagnosis.

iPericytes phagocytose myelin debris

Intrinsic pericyte dysfunction would be expected to impact vascular function before and after MS onset. However, once MS lesions form, pericytes are exposed to the complex lesion microenvironment. To determine how pericytes might respond to such stimuli, we examined the response of Control and Family RoMS iPericytes to myelin debris, hypoxia and inflammatory cytokines.

Myelin debris present within MS lesions can be phagocytosed and cleared by microglia and astrocytes [56], and there is evidence that endothelial cells can phagocytose myelin debris following spinal cord injury or EAE (Zhou et al., 2019a). While pericytes phagocytose aggregated amyloid β42 [57], it is unknown whether they support myelin clearance. To evaluate the capacity of iPericytes to phagocytose myelin and determine whether this is influenced by RoMS status, Control and Family RoMS iPericytes were plated onto pHrodo-myelin coated plates and imaged for 24 hours (**Fig. 3a**). pHrodo-myelin was detected inside iPericytes within 20 min, reflecting myelin debris uptake into acidic phagolysosomes (**Fig. 3b**). A loss of pericyte phagocytosis may partly explain why myelin debris clearance is impaired in pericyte-deficient mice following middle cerebral artery occlusion (Shibahara et al., 2020). At 24 hours, >85% of Control and Family RoMS iPericytes were pHrodo-myelin$^+$ and the rate of cell labelling was not impacted by RoMS status (**Fig. 3c**). Furthermore, the proportion of iPericyte area with pHrodo$^+$ pixels was equivalent in Control and Family RoMS iPericytes (**Fig. 3d**), indicating that Family RoMS iPericytes have a similar capacity to support myelin clearance. Importantly, Control and RoMS iPericytes maintained their normal morphology, and remained proliferative and motile after 20 hours of myelin debris exposure (**Fig. 3e-i**), indicating that myelin phagocytosis is not toxic to iPericytes.

To determine whether 44 hours of exposure to myelin debris results in transcriptional changes in Control and Family RoMS iPericytes, we performed bulk RNA sequencing. PCA of global gene expression indicated that cell line was the primary source of variation, and that exposure to myelin debris did not have a significant effect on gene expression (**Fig. 3j**). Differential gene expression analysis confirmed that myelin phagocytosis did not change the iPericyte transcriptional profile, and no genes showed evidence of an interaction effect between myelin treatment and disease status (**Fig. 3k; Fig. S4a-b**; **Data TS8-10**). These data indicate that pericytes respond differently than astrocytes, microglia, and brain microvascular endothelial cells, each of which change their proliferation rate and gene expression profile with myelin debris exposure [56,58,59]. However, our data do not rule out the possibility that the duration of myelin exposure, whether acute or sustained, could alter the pericytes, or that myelin exposure alters protein translation or induces post-translational modifications in pericytes rather than regulating gene transcription.

Hypoxia increases iPericyte proliferation, morphological remodelling, and angiogenic signalling

The MS lesion environment can become hypoxic, and this is likely to induce hypoxic injury [14,15,17,60,61]. Pericytes are early responders to brain hypoxia, commencing migration along vessels within 2 hours of a hypoxic injury [62]. To determine how hypoxia

247 impacts iPericyte behaviour and determine whether MS status alters the hypoxic
248 response, we cultured Control and Family RoMS iPericytes under normoxic or hypoxic
249 (0.5% O_2) conditions for 20 hours. Normoxic and hypoxic iPericytes incorporated EdU
250 (**Fig. 4a**), and the proportion of iPericytes that were EdU^+ increased significantly under
251 hypoxic conditions (**Fig. 4b**). This response is consistent with that of immortalised
252 retinal pericytes, which also increase their proliferation rate when cultured with <1%
253 O_2 [63]. However, the hypoxia-induced increase in proliferation was equivalent for
254 Control and Family RoMS iPericytes (**Fig. 4b**), indicating that this response is
255 unaltered by RoMS status.

256 Control and Family RoMS cells were smaller under hypoxic conditions (**Fig. 4c**), which
257 is consistent with previous *in vitro* and *in vivo* reports that hypoxia induces pericyte
258 contraction [25,64,65]. However, we also determined that more of the Control and Family
259 RoMS iPericytes adopted a spindle morphology under hypoxic conditions (**Fig. 4d-f**)
260 and organised themselves into chains of 3-8 cells (**Fig. 4g**). Only ~0.5-3.5% of
261 individual iPericytes formed chains in Control or Family RoMS cultures, yet this
262 produced a striking change in the culture appearance (**Fig. 4h**). The iPericyte chains
263 recapitulate the end-to-end organisation of pericytes along blood vessels *in vivo* [66] and
264 likely reflect their pro-angiogenic role in providing scaffolding for new vessels and
265 supporting basement membrane extension. [32]. Consistent with this idea, hypoxic
266 Control and Family RoMS iPericytes were more motile, increasing their velocity and
267 nuclear displacement (**Fig. S5a,b**), as previously reported for retinal pericytes [63].
268 These hypoxia-driven changes in pericyte motility and organisation may help explain
269 the hypervascularisation observed in MS [67,68].

270 To uncover transcriptional changes that underpin the hypoxia-induced morphological
271 and behavioural changes, we performed bulk RNA sequencing on Control and Family
272 RoMS iPericytes cultured under normoxic and hypoxic conditions. Hypoxia accounted
273 for ~24% of variation (PC1), and samples did not separate by MS status (**Fig. 4i**; **Fig.
274 S4c, Data TS11**). Our differential gene expression analysis, comparing Control and
275 Family RoMS iPericytes under hypoxic conditions revealed the same DEGs identified
276 in our baseline comparison (**Fig. S4d, Data TS12**). By comparing iPericytes cultured
277 under normoxic or hypoxic conditions, independent of MS status, we identified >1,900
278 DEGs (log fold change threshold >0.585), and most were upregulated with hypoxia
279 (**Fig. 4j, Data TS13**). Of note, the transcriptional response to hypoxia was not modified
280 by exposure to myelin debris (**Fig. S4e**). To determine whether the differential gene
281 expression was being driven by particular transcription factors that were activated
282 under hypoxic conditions, we used decoupleR to calculate transcription factor
283 enrichment scores. We determined that many of the transcriptional changes induced
284 by hypoxia, resulted from increased hypoxic inducible factor (HIF)1α activity (**Fig. S5c-
285 f**) and reduced sterol regulatory element binding (SREB) protein activity (**Fig. S5c**).
286 As the degradation of SREB transcription factors reduces the oxygen-intensive
287 process of cholesterol synthesis [69], this likely represents a pro-survival response.

288 Gene set enrichment analysis, using gene ontology (GO) biological processes,
289 identified 176 significantly enriched terms (*p-adjusted*<0.05; **Data TS14**). Consistent
290 with the morphological and behavioural changes observed in hypoxic iPericytes,

291 enriched GO terms included “response to hypoxia”, “angiogenesis” and “actin-
292 cytoskeleton organisation” (**Fig. 4k**). Notably, *ANGPTL4* was upregulated (**Fig. 4l**)
293 and was annotated to both the hypoxia and angiogenesis pathways. *ANGPTL4*
294 encodes angiopoietin-like 4, a secreted factor that regulates neovascularisation,
295 pericyte coverage, and BBB integrity [70,71]. The increased expression of *ANGTPL4*
296 and other angiogenic genes, such as *ANG* and *VEGFA*, could account for the elevated
297 iPericyte motility and altered morphology (**Fig. 4c,d,f; Fig. S5a,b**). Furthermore, the
298 upregulation of cell cycle and proliferation genes, including *PDGFB* and *CDK6*, (**Fig.**
299 **4l, Fig. S5g**), may explain the small but significant increase in iPericyte proliferation
300 with hypoxia (**Fig. 4b**). A marked increase in antigen presentation genes, including
301 MHC class I (*HLA-A, -B, -C*) (**Fig. 4l**) suggests that iPericytes are signalling increased
302 cellular stress or injury, and increasing their visibility to the immune system [72]. By
303 contrast, induction of MHC class II (*HLA-DRB1*) (**Fig. 4l**) reflects a more profound shift
304 of the cells to an acquired, non-canonical antigen-presenting state, typically restricted
305 to professional immune cells [73,74]. These changes indicate that pericytes in hypoxic
306 MS lesions may adopt an immunomodulatory phenotype capable of shaping local
307 inflammatory activity and influencing leukocyte interactions with the neurovasculature
308 [75,76].

309 Hypoxia suppressed the transcription of genes related to mitochondria and ribosome
310 function, and RNA processing (**Fig. 4k**). It also altered transcript usage for 185 genes
311 (**Fig. 4m, Data TS15**) - most of which were not differentially expressed genes (**Fig.**
312 **S5h**). As an example, hypoxia did not alter overall *MYLK* expression, but was
313 associated with a reduction in the short Telokin-encoding transcript (padj=0.0035)
314 (**Fig. S5i**). This would be predicted to promote contraction and may partly explain the
315 reduction in iPericyte size.

316 *Cytokines increase ET-1-evoked iPericyte contractility*

317 Within MS lesions, pericytes would be exposed to pro-inflammatory cytokines, such
318 as TNFα and IFNγ [77,78]. To determine how this could modify iPericytes behaviour, we
319 cultured Control and Family RoMS iPericytes with 20ng/mL TNFα, 40ng/mL IFNγ, or
320 both for 20 hours. The combined TNFα+IFNγ treatment, but not either cytokine alone,
321 reduced iPericyte proliferation, irrespective of MS status (**Fig. 5a,b**). Exposure to
322 TNFα+IFNγ also increased the cell area and perimeter of Control iPericytes (**Fig. 5c,**
323 **Fig. S6a**) such that their size resembled that of untreated Family RoMS iPericytes.
324 The failure of Family RoMS iPericytes to change in size with TNFα+IFNγ treatment
325 may reflect a ceiling effect, as they started from a larger baseline size, or an impaired
326 response to cytokine signalling. However, cytokine treatment did not produce a
327 change in overall shape, as maximum Feret diameter was unchanged (**Fig. S6b**).

328 To determine whether inflammatory cytokines influence iPericyte contractility and, by
329 extension, vascular tone, we initially exposed a Control iPericyte line to TNFα+IFNγ
330 for 0.5-20 hours, before assessing the response to ET-1. iPericyte contraction was
331 enhanced after 1 hour of TNFα+IFNγ exposure but was increased ~2-fold by 20 hours
332 (**Fig. S6c**). We therefore exposed Control and Family RoMS iPericytes to TNFα, IFNγ
333 or both for 20 hours, before measuring the ET-1-evoked contraction. As expected, the

334 Control iPericyte contraction was larger than the Family RoMS iPericyte contraction at
335 baseline (**Fig. 5d,e,f**). Exposure to TNFα or IFNγ alone increased the maximum
336 Control or Family RoMS ET-1-evoked contraction by 44.2% and 86.9% (TNFα) or
337 34.4% and 76.9% (IFNγ), respectively, although IFNγ did not reach statistical
338 significance (**Fig. 5d,e,f**). The combined TNFα+IFNγ treatment had an additive effect,
339 increasing the maximum contraction of Control and Family RoMS iPericytes by 85.5%
340 and 125.9%, respectively (**Fig. 5d,e,f**), such that the maximum contraction size
341 became equivalent for Control and Family RoMS iPericytes (**Fig. 5f**). The TNFα+IFNγ
342 stimulated iPericytes also took longer to return to their baseline size (**Fig. 5d,e**). A
343 larger and sustained pericyte contraction would greatly restrict blood flow within active
344 and smouldering lesions which would, in turn, exacerbate cellular metabolic stress,
345 promote neurodegeneration, and impede repair [79,80] (**Fig. 6**).

346 To determine how TNFα+IFNγ could exert these effects, we performed bulk RNA
347 sequencing. PCA revealed that TNFα+IFNγ exposure accounted for ~39% of gene
348 expression variation (PC1), and the samples did not cluster based on MS status (**Fig.
349 5g**). Consistent with these data, we did not detect an interaction between MS status
350 and cytokine exposure for any gene (**Fig. S6d, Data TS16**) and differential gene
351 expression analysis comparing treated Control and either Family RoMS or RoMS
352 iPericytes, only identified differences previously described for baseline conditions (**Fig.
353 S6e,f, Data TS17,18**). By contrast, TNFα+IFNγ exposure altered the expression of
354 >4,000 genes (**Fig. 5h, Data TS19**). Transcription factor analysis revealed that NFKB1
355 and IRF1 signalling were activated (**Fig. S6g,h**). NFKB1 and IRF1 activation reflects
356 the canonical responses to TNFα and IFNγ, results in the increased expression of
357 many chemokine and complement genes and is likely to result in pericytes promoting
358 leukocyte extravasation in the CNS (**Fig. S6i**). By contrast, PPARG and MYOG
359 transcriptional networks were downregulated (**Fig. S6g,h**), indicating that lipid
360 metabolism and anti-inflammatory signalling are suppressed, along with cytoskeletal
361 maintenance. Gene set enrichment revealed that cytokine treatment resulted in
362 iPericytes activating angiogenesis and antigen presentation pathways, but
363 downregulating blood circulation and calcium signalling pathways (**Fig 5i, Data TS20**).
364 Our analyses of the transcriptomics changes induced by treatment with TNFα or IFNγ
365 alone (**Fig. S7a,b, Data TS22,23**) indicate that TNFα signally largely accounts for the
366 upregulation of genes involved in blood vessel development and leukocyte migration,
367 while IFNγ modifies cytokine production and alters the innate immune response
368 (**Fig.S7a-f, Data TS24,25,26**).

369 To determine how cytokine treatment modified the ET-1 signalling pathway (**Fig. S3b**)
370 to enhance iPericyte contraction, we examined DEGs within the 'regulation of blood
371 circulation' pathway. Notably, expression of the ET-1 receptors, *EDNRA* and *EDNRB*,
372 remained unchanged (**Fig. 5j**), suggesting that the enhanced contractile response
373 resulted from modifications in downstream signalling. Consistent with this, the G-
374 protein alpha subunits that are coupled to ET-1 receptors (*GNAQ*, *GNA11*, and
375 *GNA13,* **Fig. 5j**) [81] were upregulated, along with genes that influence calcium
376 dynamics and endoplasmic reticulum calcium release, and are critical for an evoked
377 and sustained contraction (*ITPR3*, *STIM1*, *STIM2*, *ORAI1*, and *CALM1*, **Fig. 5j**). In
378 parallel, key components of the downstream actomyosin contractile apparatus were

379 elevated (*MYL12A*, *MYL12B*, *MYH11* and *ROCK1*, **Fig. S3b**). Our DTU analysis also
380 identified 517 genes (**Fig. S6j, Data TS21**). Of note, total *MYLK* gene expression was
381 decreased (**Fig. 5j**) due to selective downregulation of the telokin transcript (**Fig. S6k**).
382 Reduced telokin expression would be predicted to increase MLCK activity and myosin
383 phosphorylation to enhance contractility. These transcriptional changes indicate that
384 cytokines modify multiple downstream mediators of pericyte contraction, to drive an
385 enhanced and sustained contractile response that would restrict capillary blood flow
386 within MS lesions.

387 **Discussion**

388 Herein, we show that RoMS iPericyte experience intrinsic changes in gene expression
389 that impacts key contractile mediators, including *MYLK* (**Fig. 1**). Consistent with this,
390 RoMS iPericytes are larger, and have a reduced contractile response to the
391 vasoconstrictor, ET-1 (**Fig. 2**). While intrinsic dysfunction has the potential to initiate
392 or exacerbate MS pathogenesis, Control and Family RoMS iPericytes responded
393 similarly to MS-relevant environmental stimuli. Control and Family RoMS iPericytes
394 phagocytosed myelin debris (**Fig. 3**) and responded to hypoxia by proliferating and
395 upregulating transcripts that promote angiogenesis and contractility (**Fig. 4**). Exposure
396 to the cytokines TNFα and IFNγ resulted in larger and longer ET-1 evoked
397 contractions, that were associated with transcriptional changes expected to enhance
398 ET-1 receptor G-protein coupled signalling, intracellular calcium regulation, the
399 actomyosin contractile machinery, and MLCK activity (**Fig. 5**). These data indicate
400 that prior to MS onset, pericyte dysfunction would result in capillary dilation across the
401 CNS and likely hypoperfusion, while disease onset and lesion formation would drive
402 severe pericyte contraction and capillary constriction (**Fig. 6**).

403 Hypoperfusion and impaired neurovascular coupling may precede MS clinical onset
404 and even contribute to lesion development [27]. Individuals with clinically isolated
405 syndrome have an increased cerebral blood volume that has a longer mean transit
406 time, corresponding to reduced cerebral perfusion [13,55]. Our data suggest that this is,
407 at least in part, due to an impaired ability of pericytes to contract appropriately in
408 response to vasoactive signals. Local vasodilation is typically associated with an
409 increase in regional blood flow. However, when this is not successfully paired with the
410 vasoconstriction of capillary beds elsewhere in the cerebrovascular network, it could
411 instead result in hypoperfusion and could fail to direct blood to the most active brain
412 regions [26,82]. This is demonstrated experimentally by pericyte depletion studies, which
413 show that the loss of pericytes from across the capillary bed, results in increased
414 capillary blood volume, but global cerebral hypoperfusion [36,83]. Indeed, the focal
415 ablation of 3 proximal pericytes is sufficient to stall blood flow and cause capillary
416 regression [82]. Disturbances in blood flow can also alter endothelial cell phenotypes,
417 causing endothelial cells to upregulate genes involved in immune cell chemotaxis and
418 inflammation [84]. As iPSC-derived endothelial cells from people with MS express
419 elevated levels of the leukocyte adhesion molecules, ICAM-1 and VCAM-1 [24], pericyte
420 dysfunction that induces blood flow stalling would further exacerbate immune cell
421 adhesion to and migration across the BBB. Importantly, adhesion of leukocytes to
422 brain capillaries would further reduce blood flow [85]. Consequently, the disrupted blood

423 flow from impaired pericyte-mediated vasoconstriction and intrinsic endothelial cell
424 alterations may create a vascular environment that is more permissive to immune cell
425 infiltration, directly promoting MS development.

426 Once MS develops, it is likely that the intrinsic pericyte dysfunction becomes
427 overshadowed or masked by maladaptive responses to pathophysiological processes
428 such as hypoxia and inflammation. Although people with MS exhibit a typical cerebral
429 blood volume [55], they show reduced cerebral blood flow [7,11,12]. This reduction in blood
430 flow is often accompanied by hypervascularisation [67,68], which likely arises as a
431 secondary compensatory response to reduced blood flow and the resulting hypoxia
432 [14,15]. Our data demonstrate that exposure to 0.5% O_2 induces pericyte proliferation
433 and morphological changes that are accompanied by the upregulation of cell cycle,
434 cytoskeletal, and angiogenic genes, and this response could readily contribute to the
435 hypervascularisation observed in people with MS. In particular, the increase in spindle
436 shaped pericytes and the formation of interconnected chains likely reflect a shift
437 toward a pro-angiogenic state. We hypothesise that this is a monoculture *in vitro*
438 presentation of the scaffolding role pericytes have to support endothelial tip cells, and
439 direct new blood vessel formation *in vivo* [32,33,86]. Despite higher vessel densities in the
440 MS brain [67,68], hypoperfusion is still observed, likely due to chronic inflammation
441 resulting in poor vessel development, hyper-constriction via pericytes and damage.

442 In MS lesions, the elevated levels of TNFα [78] and IFNγ [77] would significant impair
443 pericyte function. When iPericytes were exposed to TNFα [78] and IFNγ that
444 upregulated genes involved in G-protein, calcium and actomyosin signalling, and
445 experienced larger and longer ET-1 evoked contractions. These cytokine-induced
446 changes to pericyte function could readily explain the narrowed capillaries, reduced
447 blood flow and heterogenous capillary transit times reported within MS lesions [18,87,88].
448 However, the ability of cytokines to increase the size and duration of pericyte
449 contraction also has implications for neurovascular dysfunction in other
450 neuroinflammatory conditions, including stroke, where it likely contributes to the no-
451 reflow phenomenon [65,89]. As cytokine-stimulated iPericytes also increase their
452 expression of chemokine genes, they may actively promote leukocyte recruitment to
453 the CNS, which could promote capillary plugging and exacerbate hypoperfusion [85].

454 In people with MS, cerebral blood flow is inversely associated with T1 lesion volume,
455 neuroinflammation, and serum neurofilament light chain (neurodegeneration) [8,79,80],
456 indicating that blood flow restoration could have a significant impact on
457 neuroprotection and repair. The potential benefit of restoring perfusion is highlighted
458 by studies in EAE and Alzheimer's disease (APP^{NL-G-F}) mice, where treatment with
459 the CNS-selective vasodilator nimodipine improved perfusion and reduced
460 demyelination (EAE only), hypoxia, immune cell stalling, and neurological deficits [90,91].
461 These findings underscore the importance of targeting pericyte function and cerebral
462 perfusion as a therapeutic strategy in MS.

463 **Methods**

464 *Resource availability*

465 Further information and requests for data or resources related to this publication
466 should be directed to the corresponding author.

467 iPSC line generation and availability

468 All iPSC lines used in this study were generated for our MS Stem biobank (Menzies
469 Institute for Medical Research) and can be purchased from
470 https://msresearchflagship.org.au/researchers/ms-stem. The iPSC lines were
471 generated and characterised as previously described [40,41]. The generation and use of
472 each iPSC line was approved by the University of Tasmania Human Research Ethics
473 Committee (approvals 16915 and 30092). All study participants provided informed
474 consent for the blood sample collection, iPSC generation, differentiation, and genetic
475 data sharing conducted as part of this project. n=10 Control, n=4 Family [40] and n=8
476 RoMS iPSC lines (**Table 1**) were used in this study.

477 iPSC culture and iPericyte differentiation

478 iPSCs were cultured on Matrigel® (Corning) coated 60mm Nunclon Delta plates
479 (ThermoFisher) in mTeSR1™ Plus medium (StemCell Technologies, cat.#100-0276).
480 iPSCs were passaged every 6-8 days and the medium exchanged every 2 days. One
481 day prior to passaging, areas of spontaneous differentiation were removed by scraping
482 the plate with a 200µl pipette tip and washing with DMEM/F12 (ThermoFisher). For
483 passaging, cells were dissociated into clumps by incubating cells in ReLeSR™
484 (StemCell Technologies, cat.#100-0484). iPericytes were generated as previously
485 described [39], by plating iPSCs in 60mm matrigel-coated plates. After 2 days, the
486 medium was exchanged for STEMdiff™ Mesoderm Induction Medium (MIM; StemCell
487 Technologies, #05221), replaced daily for 5 days, and complete pericyte medium
488 (CPM) containing pericyte growth supplement and fetal bovine serum (FBS; ScienCell,
489 #1201), replaced daily for the subsequent 5 days. On day 10, the cells were
490 dissociated with Accutase® (StemCell Technologies, #07922) and plated in uncoated
491 6-well plates at a density of 5 x 10^4 per cm^2. The medium was replaced every 48h,
492 and the cells passaged at ~80% confluency (~5-7 days). iPericytes were frozen in
493 CPM with 10% dimethyl sulfoxide and stored in liquid nitrogen. iPericytes were thawed
494 into CPM and culture for 2 weeks prior to use in experiments. Passage 3-7 iPericytes
495 were used for experiments.

496 Immunocytochemistry

497 Pericytes were grown to ~25% confluency in 24 well plates and fixed with cold 4%
498 (w/v) paraformaldehyde (Sigma) in PBS for 15 mins at 21°C. Cells were washed with
499 PBS and then incubated in blocking solution (10% Tween-20 / 2% FBS in PBS) for 30
500 minutes at 21°C. Primary antibodies (goat anti-PDGFRβ , R&D Systems AF385,
501 RRID:AB_777165; rabbit anti-CD13, Abcam Ab108310, RRID:AB_10866195;) were
502 diluted in the blocking solution and applied overnight at 4°C, and the plates placed on
503 an orbital shaker. Cells were washed thrice in PBS before secondary antibodies (Alexa
504 Fluor 488-conjugated donkey anti-rabbit; Alexa Fluor 647-conjugated donkey anti-
505 goat) and Hoechst 33342, diluted in blocking solution, were applied for 2 hours at
506 21°C. Cells were washed thrice in PBS and maintained in PBS for imaging.

507 Fluorescent Microscopy

508 All fluorescent images were acquired using an iXon Ultra 888 EMCCD camera
509 mounted on an inverted Nikon Eclipse Ti microscope, with imaging performed blinded
510 to disease status and/or treatment group. Either a Plan Apo 10× or Plan Apo VC 20×
511 DIC N2 objective was used. Illumination was provided by a SPECTRA X light source
512 equipped with Semrock 387/11, 485/20, 560/25, and 650/13 excitation filters, a
513 Semrock FF410/504/582/669 dichroic mirror, and Semrock 440/521/607/700 emission
514 filters. Uniform exposure times were maintained across all images within each
515 experiment.

516 RNA sequencing

517 iPSCs were seeded on 60mm plates and cultured to ~75% confluency prior to
518 collection. Pericytes were seeded on 6-well plates (300,000 cells per well) and cultured
519 for 44 hours prior to collection. Pericytes were exposed to hypoxic conditions or
520 cytokine treatment for 20 hours. They were exposed to myelin debris for 44 hours.
521 Cells were dissociated using Accutase, washed in cold DPBS and lysed using RLT
522 buffer (Qiagen). The lysate was stored at -20°C and thawed on ice for RNA extraction
523 using the RNeasy Mini Kit, following the manufacturer's instructions (Qiagen, #74106).
524 Briefly, samples were transferred to RNeasy spin columns, DNA removed by treatment
525 with DNase (Qiagen, #79254) and RNA eluted in 40µl of RNase free water. RNA
526 concentration and integrity were evaluated using the Agilent 4200 Tapestation system.
527 Briefly, 5µl of RNA ScreenTape Sample Buffer (Agilent, #5067-5577) and 1µl of RNA
528 sample or ladder were combined by vortexing at 2,000rpm for 1 minute using an IKA
529 vortex. Samples were incubated at 72°C for 3 minutes, placed on ice for 2 minutes,
530 loaded into the TapeStation and run on RNA ScreenTape (Agilent, #5067-5576) via
531 electrophoresis. Samples with > 20ng/µL RNA and a RNA integrity number (RIN) > 8
532 were sent to the Australian Genome Research Facility for bulk RNA sequencing to a
533 minimum depth of 20 or 50 million reads with 150 base paired end lengths. Libraries
534 were generated with the Illumina Stranded mRNA workflow with polyA capture. Raw
535 RNA sequencing data is available for download from the European Genome Phenome
536 Archive (accession to be provided for publication) or, for data generated from a limited
537 number of the iPSC lines, by reasonable request to the corresponding author.

538 Re-analysis of publicly available RNAseq datasets

539 HBVP, iPSC and iPericyte raw bulk RNA sequencing data from King, et al. [39] were
540 downloaded from GEO (accession GSE252046) and the European Genome Phenome
541 Archive (accession EGAD50000000255).

542 RNA data processing

543 Raw sequencing data were processed using nf-core/rnaseq v3.12.0 [92], and a nf-core
544 workflow executed with Nextflow v.23.04.2. Initially, the sequencing adapter (5'-
545 CTGTCTCTTATACACATCT - 3') was trimmed from each read and 1 base pair
546 removed from the 5' end of each read using TrimGalore [93]. A read quality Phred score
547 threshold of 20 was used to remove low quality reads. Reads <25 base pairs after
548 trimming were discarded. The quality of the sequencing data was evaluated using

549 FastQC (v.0.11.9), and all data met the necessary quality metrics for analysis. Gene
550 expression was quantified using Salmon in mapping-based mode (v.1.10.1) with the
551 *Homo sapiens* (Hg38) reference transcriptome. The sequencing library type was
552 inward stranded reverse (ISR). Within Salmon, --seqBias and --gcBias were employed
553 to enable Salmon to learn and correct for sequence-specific biases and fragment-level
554 GC biases, respectively. The result of this analysis was per sample quantification of
555 transcript expression.

556 Differential gene expression analysis, differential transcript usage and gene set
557 enrichment

558 Differential gene expression analysis was performed using DESeq2 [94] (v1.42.0).
559 Tximport [95] (v.1.30.0) was used to import transcript-level abundance into R (v.4.4.2)
560 and summarise transcript abundance to the gene-level. Genes with <10-100 reads
561 across each group were filtered out. A first pass differential gene expression was
562 performed comparing gene expression levels between the experimental groups being
563 tested. Factors of unwanted variation were estimated and included as covariates in
564 the model using RUVSeq [96] (v1.36.0) as required. A *p*-value of 0.5 was used to define
565 a set of genes not differentially expressed in the first pass analysis for use as in-silico
566 empirical negative control genes in RUVSeq. Differential gene expression was tested
567 under a hypothesis of $\log_2$ fold changes > 0.1 for Control vs RoMS testing and 0.585
568 (corresponding to a 1.5-fold change in expression) for treatment testing, with a false
569 discovery rate threshold of alpha <0.05. When examining interaction effects between
570 disease status and treatment a $\log_2$ fold change threshold of > 0.1 was used. When
571 examining interaction effects between TNFα and IFNγ treatment a $\log_2$ fold change
572 threshold of > 0.585 was used. Each differential gene expression analysis was
573 visualised using EnhancedVolcano [97] (v.1.20.0), pheatmap [98] (v.1.012) or ggplot2 [99]
574 (v.3.5.1). Differential transcript usage analysis was performed using
575 IsoformSwitchAnalyzer (v.2.6.0) [100] with a gene expression cut off of 10 and isoform
576 expression cut off of 3. DEXSeq (v.1.52.0) [101] was used for DTU statistical testing.
577 Gene set enrichment analysis (GSEA) was completed using clusterProfiler (v.4.14.4)
578 [102]. Transcription factor analyses were completed using decoupleR [103] (v.2.8.0).

579 EdU proliferation assay

580 EdU assays were performed as previously described [39,104], between passage 4 and 5.
581 Briefly, pericytes were plated into 96-well plates at 5,000 cells per well and left to
582 adhere overnight. The following day, the medium was replaced with CPM containing
583 1μM EdU (ThermoFisher) and the cells incubated for 20 hours. The medium was then
584 removed and the cells fixed with cold 4% paraformaldehyde in PBS for 15 minutes at
585 21°C and washed with PBS. EdU incorporation was detected using the Click iT EdU
586 proliferation kit with Alexa Fluor 647 dye (ThermoFisher, #C10340) according to the
587 manufacturer's instructions, and nuclei identified by incubation with Hoechst 33342
588 (ThermoFisher; #C10340; 1:1000) for 15 minutes at 21°C. Hoechst 33342^+ nuclei were
589 identified in each image and scored as EdU^+ when EdU fluorescence was also in the
590 nucleus. The percentage (%) of iPericytes that had incorporated EdU was calculated
591 as (EdU^+ Hoechst 33342^+ nuclei / total Hoechst 33342^+ nuclei) x 100. EdU assays

592 were performed on iPericytes cultured in a standard incubator, on myelin-coated
593 plates, under hypoxic conditions (0.5% O_2), on myelin coated plates in hypoxic
594 conditions or with TNFα and/or IFNγ treatment.

595 Motility assay

596 5,000 pericytes were plated per well in 96-well plates coated with poly-L-lysine ±
597 pHrodo conjugated myelin (3µg/cm^2). Pericytes were incubated for 24 hours before
598 being transferred to a Nikon Eclipse Ti2 microscope in a cage incubator (Okolab)
599 maintained at 5% CO_2 and 37°C. To assess motility under hypoxic conditions,
600 pericytes were placed in the cage incubator maintained at 1% O_2, 5% CO_2 and 37°C
601 for 24 hours prior to imaging. Phase contrast images were collected every 3 minutes
602 for 1 hour. Individual cell nuclei were annotated in each frame using QuPath (v.5.1)
603 [105]. Cell velocity was calculated as the change in XY coordinates of the cell nucleus
604 between frames for each individual cell, divided by the change in time (µm/min).
605 Nucleus displacement was calculated as the change in XY of the nucleus coordinates
606 between the first and last frames (1 hour).

607 Morphology assay

608 Pericytes were plated into 96-well plates at 5,000 cells per well and cultured for 2 days
609 prior to fixation with 4% paraformaldehyde in PBS for 15 minutes at 21°C, and washed
610 with PBS. Phase contrast images were taken on a Nikon Eclipse Ti2 microscope and
611 the outer edge of each pericyte was traced using QuPath (v.5.1) and the annotation
612 tool. Each pericyte was manually classified using the morphological subtypes
613 described by Brown et al. (2023). Cell area, cell perimeter and max diameter were
614 extracted from each pericyte tracing using the Calculate Features tool. Morphological
615 assessments were performed on iPericytes cultured in a standard incubator, on
616 myelin-coated plates, under hypoxic conditions (0.5% O_2), or exposed to TNFα
617 (20ng/mL) and/or IFNγ (40ng/mL).

618 For pericyte chain analysis, pericytes were stained with Hoechst 33342 prior to
619 imaging. Pericytes were determined to be in a chain arrangement if 3 or more cells
620 lined up end to end and were physically touching.

621 Attachment assay

622 Pericytes were plated into 96-well plates at 5,000 cells per well and immediately
623 transferred to a Nikon Eclipse Ti2 microscope in a cage incubator (Okolab) maintained
624 at 5% CO_2 and 37°C. Phase contrase images were collected every 10 minutes for 2
625 hours, and then every hour for 3 hours. The percentage (%) of pericytes that had
626 attached to the plate was quantified in each video frame.

627 Contractility and relaxation assays

628 An xCELLigence real-time cell analysis electrical impedance assay was used to
629 quantify pericyte contractility or relaxation, as previously published [39,53]. Briefly, 10,000
630 pericytes were plated in each well of an e-plate (ACEA Biosciences, cat.#0546983000)
631 with 150µL of CPM, and left to adhere overnight. For contractility, 50nM of ET-1was
632 added to 10µL of CPM, for each well to be assessed. The e-plate was quickly removed

633 from the incubator, 10µL of CPM alone (diluent) or diluted endothelin-1 (50µM) added
634 to each well, and then placed in the xCELLigence system, maintained at 37°C and 5%
635 CO_2. For relaxation, 10µL of CPM alone (diluent) or adenosine (10µM) was used, but
636 the E-plate was removed from incubator for 2 minutes prior adding CPM or adenosine
637 to induce a contraction in response to the change in environmental conditions. The e-
638 plate was then placed in the xCELLigence system. Electrical impedance, expressed
639 as cell index, was measured every minute for 2 hours. Normalised cell index was
640 calculated by normalising the raw cell index to the cell index value at the first timepoint.
641 For cytokine contractility experiments, pericytes were plated into e-plates and allowed
642 to attach for 3 hours prior to exchanging medium with cytokine containing medium.
643 Pericytes were then incubated for 20 hours prior to contractility assessment.

644 For live imaging contractility assessment, pericytes from one Control cell line was
645 plated into 96-well plates at 5,000 cells per well and cultured for 24 hours. Cells were
646 then transferred to a Nikon Eclipse Ti2 microscope in a cage incubator (Okolab)
647 maintained at 5% CO_2 and 37°C. Pericytes were incubated for 1 hour to ensure
648 stability of pericyte contractile state, minimising the effects of moving the pericytes
649 from the culture incubator to the microscope incubator. While the cells were
650 maintained in the incubator, 10µL of CPM alone (diluent) or diluted endothelin-1 was
651 added to each well. Cells were imaged every minute for an hour and frames 1, 20 and
652 60 used for morphological analysis. The outer edge of each pericyte was traced using
653 QuPath (v.5.1) using the annotation tool to measure cell area at each timepoint. To
654 assess changes in contractility, cell area measurements at frames 20 and 60 were
655 normalised to each individual cell area at frame 1 and expressed as a percentage.

656 Myelin extraction and pHrodo-bead conjugation

657 Animal experiments were approved by the University of Tasmania Institutional
658 Biosafety Committee and Animal Ethics Committee (A0028218 and A0028287) and
659 were carried out in accordance with the Australian Code of Practice for the Care and
660 Use of Animals for Scientific Purposes (8th edition). Mice were housed in Optimice®
661 microisolator cages (2-5 per cage, Animal Care Systems, Colorado, USA) maintained
662 at 21 ± 2°C and followed a 12-hour light/dark cycle. Mice had access to standard
663 rodent chow (Barrastoc rat and mouse pellets) and water *ad libitum*.

664 Crude mouse myelin extraction was performed as previously described [106]. Briefly,
665 n=2 ~1 year old C57BL/6 mice (1 male and 1 female) were euthanised by CO_2
666 asphyxiation and the brains dissected into a sterile 6cm cell culture dish containing
667 0.32M sucrose in 1M Tris-HCl. Brain tissue was chopped into ~0.5mm^3 pieces and
668 transferred to a sterile hand-held rotary homogeniser containing ~10mL of 0.32M
669 sucrose in 1M Tris-HCl. Brain tissue was homogenised and diluted into 0.32M sucrose
670 in 1M Tris-HCl. The tissue homogenate was then placed on top of 0.83M sucrose in
671 1M TrisHCl solution in polypropylene ultracentrifuge tubes (Beckman Coutler,
672 cat.#331372). The tissue was centrifuged at 100,000g for 45 minutes at 4°C, so that
673 the myelin debris accumulated at the interface of the two sucrose concentrations.
674 Myelin debris was collected, placed in new ultracentrifuge tubes and centrifuged again.
675 The resulting myelin pellet was washed by resuspension in 1M Tris-HCl buffer,

676 centrifugation, resuspension in sterile PBS, centrifugation before being resuspended
677 again in PBS and stored at -80°C.

678 Myelin was ultrasonicated using a Bioruptor® Plus sonication device (20x, 20 seconds
679 on, 20 seconds off) in 1.5 mL Bioruptor® Plus TPX microtubes (Diagenode,
680 cat.#C30010010-300). The myelin was then resuspended in 0.1M sodium bicarbonate
681 buffer (pH 8.4), prior to adding 10mM of pHrodo iFL Red STP ester, amine reactive
682 dye (ThermoFisher Scientific, cat.#P36011) in DMSO at a concentration of 0.1µL per
683 µg of myelin for 1 hour at 21°C in the dark. Labelled myelin was centrifuged at 22,000g
684 for 5 minutes at 4°C and resuspended in sterile PBS to wash away excess dye. Finally,
685 the labelled myelin was centrifuged at 22,000g for 5 minutes at 4°C, resuspended in
686 sterile PBS at a concentration of 2µg per µL, and sonicated (10x, 20 seconds on, 20
687 seconds off), before storage at -20°C for use in experiments.

688 Myelin phagocytosis assay

689 96-well plates were incubated with poly-L-lysine (0.001%, Merck, cat.#P4707) ±
690 pHrodo-myelin (3µg/cm^2) for 2 days before plates were washed with DPBS and the
691 pericytes seeded at 5,000 cells per well. Seeded plates were placed in a cage
692 incubator (Okolab) maintained at 5% CO_2 and 37°C. Phase contrast and fluorescent
693 images were taken every 20 minutes for 24 hours. The percentage (%) of pericytes,
694 identified by DIC imaging, that had pHrodo$^+$ puncta, indicative of myelin phagocytosis,
695 was quantified in each video frame. From images collected at the 24-hour timepoint,
696 the outer edge of individual pericytes was traced using QuPath (v.5.1), and the area
697 containing pHrodo labelling was calculated and expressed as a percentage of the total
698 cell area.

699 Inducing hypoxia

700 To model hypoxic conditions, iPericytes cultured on regular or myelin coated plates,
701 were incubated in a hypoxia chamber (StemCell Technologies, #27310) with a
702 portable oxygen monitor. A 100mm petri dish containing 5mL of dH_2O was placed in
703 the bottom of the chamber to maintain humidity. The chamber was flushed with 5%
704 CO_2 in N_2 until the oxygen level stabilised at 0.5%. Cells under normoxic conditions
705 were place in an identical but unsealed chamber. The chambers were maintained
706 inside an incubator at 37ºC for 20 hours.

707 Cytokine exposure

708 To model inflammatory MS lesion-like conditions, iPericytes were incubated in
709 cytokine containing media. iPericytes were cultured in TNFα (20ng/mL; StemCell
710 Technologies, #78157.1) and/or IFNγ (40ng/mL; StemCell Technologies, #78141.1)
711 containing CPM for 20 hours unless otherwise specified.

712 Statistical analyses

713 All quantification was performed blind to treatment condition and MS status. Statistical
714 analyses were performed in R (v.4.4.2). All data unless otherwise stated were
715 analysed by restricted maximum likelihood (REML) mixed models with cell line as a
716 random effect (lme4 package v.1.1-35.1). Multiple comparison post hoc (Tukey

method) tests were performed utilising the Kenward-Roger method for degrees of freedom (emmeans R v.1.8.9). Analysis of proportional data was performed using a binomial generalised linear mixed model. Statistical significance was set as $p<0.05$ and data are presented as group means ± SEM for column and line graphs, and median ± interquartile range for boxplots.

Acknowledgements:

This research was supported by grants from the Medical Research Future Fund (EPCD0008), the National Health and Medical Research Council (NHMRC; 2030057; 2035302; APP1163384), MS Australia (118273, 20-137, 23-0202, 25-0338) and the Irene Phelps Charitable Trust. A.J.F was supported by an Australian Research Training Program scholarship and a Menzies Institute for Medical Research Philanthropic Fellowship. K.M.Y was supported by a Senior Research Fellowship from MS Australia (21-3-023). J.L.F and N.B.B were supported by Research Fellowships from MS Australia (23-PDF-0121, 22-4-097). B.V.T was supported by an NHMRC Investigator Award (GNT3008389). J.M.C was supported by Tasmanian Graduate Research scholarships.

Author Contributions:

A.J.F: methodology; funding acquisition; validation; investigation; formal analysis; visualisation; writing – original draft; writing – review and editing. N.E.K: methodology; validation; investigation; writing – review and editing. A.G: investigation. R.A.M: investigation; formal analysis; writing – review and editing. J.M.C: methodology; investigation; writing – review and editing. K.P.B: methodology; supervision. B.V.T: conceptualisation; funding acquisition. B.A.S: funding acquisition; methodology; supervision; writing – review and editing. J.L.F: conceptualisation; investigation; funding acquisition; methodology; supervision; writing – review and editing. N.B.B: conceptualisation; funding acquisition; methodology; formal analysis; visualisation; supervision; writing – review and editing. K.M.Y: conceptualisation; funding acquisition; methodology; visualisation; supervision; writing – original draft; writing – review and editing.

Declaration of Interests:

The authors declare no competing interests.

References

1 Woo, M. S., Engler, J. B. & Friese, M. A. The neuropathobiology of multiple sclerosis. *Nat Rev Neurosci* **25**, 493–513 (2024). https://doi.org/10.1038/s41583-024-00823-z

2 Cramer, S. P., Simonsen, H., Frederiksen, J. L., Rostrup, E. & Larsson, H. B. Abnormal blood-brain barrier permeability in normal appearing white matter in multiple sclerosis investigated by MRI. *Neuroimage Clin* **4**, 182–189 (2014). https://doi.org/10.1016/j.nicl.2013.12.001

3 Plumb, J., Mcquaid, S., Mirakhur, M. & Kirk, J. Abnormal Endothelial Tight Junctions in Active Lesions and Normal-appearing White Matter in Multiple Sclerosis. *Brain Pathology* **12**, 154–169 (2002). https://doi.org/10.1111/j.1750-3639.2002.tb00430.x

4 Zierfuss, B., Larochelle, C. & Prat, A. Blood-brain barrier dysfunction in multiple sclerosis: causes, consequences, and potential effects of therapies. *Lancet Neurol* **23**, 95–109 (2024). https://doi.org/10.1016/S1474-4422(23)00377-0

5 Leech, S., Kirk, J., Plumb, J. & McQuaid, S. Persistent endothelial abnormalities and blood-brain barrier leak in primary and secondary progressive multiple sclerosis. *Neuropathol Appl Neurobiol* **33**, 86–98 (2007). https://doi.org/10.1111/j.1365-2990.2006.00781.x

6 Stickland, R. *et al.* Neurovascular Coupling During Visual Stimulation in Multiple Sclerosis: A MEG-fMRI Study. *Neuroscience* **403**, 54–69 (2019). https://doi.org/10.1016/j.neuroscience.2018.03.018

7 Hojjat, S. P. *et al.* Regional reduction in cortical blood flow among cognitively impaired adults with relapsing-remitting multiple sclerosis patients. *Mult Scler* **22**, 1421–1428 (2016). https://doi.org/10.1177/1352458515622696

8 Mascali, D. *et al.* Pathophysiology of multiple sclerosis damage and repair: Linking cerebral hypoperfusion to the development of irreversible tissue loss in multiple sclerosis using magnetic resonance imaging. *Eur J Neurol* **30**, 2348–2356 (2023). https://doi.org/10.1111/ene.15827

9 de la Pena, M. J. *et al.* Early perfusion changes in multiple sclerosis patients as assessed by MRI using arterial spin labeling. *Acta Radiol Open* **8**, 2058460119894214 (2019). https://doi.org/10.1177/2058460119894214

10 Chandler, H. L. *et al.* Reduced brain oxygen metabolism in patients with multiple sclerosis: Evidence from dual-calibrated functional MRI. *J Cereb Blood Flow Metab* **43**, 115–128 (2023). https://doi.org/10.1177/0271678X221121849

11 Adhya, S. *et al.* Pattern of hemodynamic impairment in multiple sclerosis: dynamic susceptibility contrast perfusion MR imaging at 3.0 T. *Neuroimage* **33**, 1029–1035 (2006). https://doi.org/10.1016/j.neuroimage.2006.08.008

12 Law, M. *et al.* Microvascular Abnormality in Relapsing-Remitting Multiple Sclerosis: Perfusion MR Imaging Findings in Normal-appearing White Matter. *Radiology* **231** (2004). https://doi.org/10.1148/radiol.2313030996

13 Varga, A. W. *et al.* White matter hemodynamic abnormalities precede sub-cortical gray matter changes in multiple sclerosis. *J Neurol Sci* **282**, 28–33 (2009). https://doi.org/10.1016/j.jns.2008.12.036

14 Yang, R. & Dunn, J. F. Reduced cortical microvascular oxygenation in multiple sclerosis: a blinded, case-controlled study using a novel quantitative near-infrared spectroscopy method. *Sci Rep* **5**, 16477 (2015). https://doi.org/10.1038/srep16477

15 Williams, T., Lange, F., Smith, K. J., Tachtsidis, I. & Chataway, J. Investigating cortical hypoxia in multiple sclerosis via time-domain near-infrared spectroscopy. *Ann Clin Transl Neurol* **11**, 2372–2381 (2024). https://doi.org/10.1002/acn3.52150

16 Burtscher, J. *et al.* Hypoxia in multiple sclerosis. *Redox Biol* **83**, 103666 (2025). https://doi.org/10.1016/j.redox.2025.103666

17 Adingupu, D. D. *et al.* Temporal Pattern of Cortical Hypoxia in Multiple Sclerosis and Its Significance on Neuropsychological and Clinical Measures of Disability. *Ann Neurol* **94**, 1067–1079 (2023). https://doi.org/10.1002/ana.26769

18 Sundvall, L. *et al.* Neurodegeneration and energy depletion in MS: Links between tissue integrity loss and microvascular changes in white matter disease. *Neuroimage Rep* **6**, 100309 (2026). https://doi.org/10.1016/j.ynirp.2025.100309

19 Stamenkovic, S. *et al.* Impaired capillary-venous drainage contributes to gliosis and demyelination in mouse white matter during aging. *Nat Neurosci* **28**, 1868–1882 (2025). https://doi.org/10.1038/s41593-025-02023-z

20 Rondelli, A. *Impact of hypoxia on remyelination in a mouse model of Multiple Sclerosis* Doctor of Philosophy thesis, The University of Edinburgh, (2020).

21 International Multiple Sclerosis Genetics Consortium. Multiple sclerosis genomic map implicates peripheral immune cells and microglia in susceptibility. *Science* **365**, eaav7188 (2019). https://doi.org/10.1126/science.aav7188

22 Absinta, M. *et al.* A lymphocyte–microglia–astrocyte axis in chronic active multiple sclerosis. *Nature* **597**, 709–714 (2021). https://doi.org/10.1038/s41586-021-03892-7

23 Fortune, A. J., Fletcher, J. L., Blackburn, N. B. & Young, K. M. Using MS induced pluripotent stem cells to investigate MS aetiology. *Multiple Sclerosis and Related Disorders* **63**, 103839 (2022). https://doi.org/10.1016/j.msard.2022.103839

24 Nishihara, H. *et al.* Intrinsic blood–brain barrier dysfunction contributes to multiple sclerosis pathogenesis. *Brain* **145**, 4334–4348 (2022). https://doi.org/10.1093/brain/awac019

25 Hall, C. N. *et al.* Capillary pericytes regulate cerebral blood flow in health and disease. *Nature* **508**, 55–60 (2014). https://doi.org/10.1038/nature13165

26 Gonzales, A. L. *et al.* Contractile pericytes determine the direction of blood flow at capillary junctions. *Proc Natl Acad Sci U S A* **117**, 27022–27033 (2020). https://doi.org/10.1073/pnas.1922755117

27 Cashion, J. M., Young, K. M. & Sutherland, B. A. How does neurovascular unit dysfunction contribute to multiple sclerosis? *Neurobiol Dis* **178**, 106028 (2023). https://doi.org/10.1016/j.nbd.2023.106028

28 Brown, L. S. *et al.* Pericytes and Neurovascular Function in the Healthy and Diseased Brain. *Front Cell Neurosci* **13**, 282 (2019). https://doi.org/10.3389/fncel.2019.00282

29 Guo, X. *et al.* Atp13a5 Marker Reveals Pericyte Specification in the Mouse Central Nervous System. *J Neurosci* **44** (2024). https://doi.org/10.1523/JNEUROSCI.0727-24.2024

30 Kaushik, D. K., Bhattacharya, A., Lozinski, B. M. & Wee Yong, V. Pericytes as mediators of infiltration of macrophages in multiple sclerosis. *J Neuroinflammation* **18**, 301 (2021). https://doi.org/10.1186/s12974-021-02358-x

31 Dias, D. O. *et al.* Pericyte-derived fibrotic scarring is conserved across diverse central nervous system lesions. *Nature Communications* **12** (2021). https://doi.org/10.1038/s41467-021-25585-5

32 Ribatti, D., Nico, B. & Crivellato, E. The role of pericytes in angiogenesis. *Int J Dev Biol* **55**, 261–268 (2011). https://doi.org/10.1387/ijdb.103167dr

33 Ren, S. Y. *et al.* Growth hormone promotes myelin repair after chronic hypoxia via triggering pericyte-dependent angiogenesis. *Neuron* **112**, 2177–2196 e2176 (2024). https://doi.org/10.1016/j.neuron.2024.03.026

34 Torok, O. *et al.* Pericytes regulate vascular immune homeostasis in the CNS. *Proc Natl Acad Sci U S A* **118** (2021). https://doi.org/10.1073/pnas.2016587118

35 Armulik, A. *et al.* Pericytes regulate the blood–brain barrier. *Nature* **468**, 557–561 (2010). https://doi.org/10.1038/nature09522

36 Cashion, J. M. *et al.* Pericyte ablation causes hypoactivity and reactive gliosis in adult mice. *Brain Behav Immun* (2025). https://doi.org/10.1016/j.bbi.2024.10.014

37 Yousefi, M. *et al.* Reactive pericytes lead to microvascular dysfunction and cortical neurodegeneration during experimental autoimmune encephalomyelitis. *Biorxiv* (2025). https://doi.org/10.1101/2025.02.17.638582

38 Faal, T. *et al.* Induction of Mesoderm and Neural Crest-Derived Pericytes from Human Pluripotent Stem Cells to Study Blood-Brain Barrier Interactions. *Stem Cell Reports* **12**, 451–460 (2019). https://doi.org/10.1016/j.stemcr.2019.01.005

39 King, N. E. *et al.* Induced pluripotent stem cell derived pericytes respond to mediators of proliferation and contractility. *Stem Cell Res Ther* **15**, 59 (2024). https://doi.org/10.1186/s13287-024-03671-x

40 Fortune, A. J. *et al.* Generation and characterisation of four multiple sclerosis iPSC lines from a single family. *Stem Cell Res* **62**, 102828 (2022). https://doi.org/10.1016/j.scr.2022.102828

41 Mehta, A. *et al.* Generation of MNZTASi001-A, a human pluripotent stem cell line from a person with primary progressive multiple sclerosis. *Stem Cell Research* **57**, 102568 (2021). https://doi.org/10.1016/j.scr.2021.102568

42 Sancho, M., Klug, N. R., Harraz, O. F., Hill-Eubanks, D. & Nelson, M. T. Distinct potassium channel types in brain capillary pericytes. *Biophys J* **123**, 2110–2121 (2024). https://doi.org/10.1016/j.bpj.2024.03.004

43 Harraz, O. F. *et al.* Ca(V)3.2 channels and the induction of negative feedback in cerebral arteries. *Circ Res* **115**, 650–661 (2014). https://doi.org/10.1161/CIRCRESAHA.114.304056

44 Gateva, G. *et al.* Tropomyosin Isoforms Specify Functionally Distinct Actin Filament Populations In Vitro. *Curr Biol* **27**, 705–713 (2017). https://doi.org/10.1016/j.cub.2017.01.018

45 Sachan, A. *et al.* Rnd3 regulates cell morphodynamics by spatial restriction of cell contraction signaling *Biorxiv* (2025). https://doi.org/10.1101/2025.09.23.677979

46 Wu, N. *et al.* RND3 attenuates oxidative stress and vascular remodeling in spontaneously hypertensive rat via inhibiting ROCK1 signaling. *Redox Biol* **48**, 102204 (2021). https://doi.org/10.1016/j.redox.2021.102204

47 Nicaise, A. M. *et al.* iPS-derived neural progenitor cells from PPMS patients reveal defect in myelin injury response. *Experimental Neurology* **288**, 114–121 (2017). https://doi.org/https://doi.org/10.1016/j.expneurol.2016.11.012

48 Nicaise, A. M. *et al.* Cellular senescence in progenitor cells contributes to diminished remyelination potential in progressive multiple sclerosis. *Proceedings of the National Academy of Sciences* **116**, 9030–9039 (2019). https://doi.org/10.1073/pnas.1818348116

49 Khromov, A. S. *et al.* Smooth muscle of telokin-deficient mice exhibits increased sensitivity to Ca 2+ and decreased cGMP-induced relaxation. *Proc Natl Acad Sci U S A* **103**, 2440–2445 (2006).

50 Herring, B. P., El-Mounayri, O., Gallagher, P. J., Yin, F. & Zhou, J. Regulation of myosin light chain kinase and telokin expression in smooth muscle tissues. *Am J Physiol Cell Physiol* **291**, C817–827 (2006). https://doi.org/10.1152/ajpcell.00198.2006

51 Brown, L. S. *et al.* Brain pericytes in culture display diverse morphological and functional phenotypes. *Cell Biol Toxicol* **39**, 2999–3014 (2023). https://doi.org/10.1007/s10565-023-09814-9

52 Kutcher, M. E., Kolyada, A. Y., Surks, H. K. & Herman, I. M. Pericyte Rho GTPase mediates both pericyte contractile phenotype and capillary endothelial growth state. *Am J Pathol* **171**, 693–701 (2007). https://doi.org/10.2353/ajpath.2007.070102

53 Neuhaus, A. A., Couch, Y., Sutherland, B. A. & Buchan, A. M. Novel method to study pericyte contractility and responses to ischaemia in vitro using electrical impedance. *J Cereb Blood Flow Metab* **37**, 2013–2024 (2017). https://doi.org/10.1177/0271678X16659495

54 Faraco, G. *et al.* Circulating endothelin-1 alters critical mechanisms regulating cerebral microcirculation. *Hypertension* **62**, 759–766 (2013). https://doi.org/10.1161/HYPERTENSIONAHA.113.01761

55 Papadaki, E. Z. *et al.* White matter and deep gray matter hemodynamic changes in multiple sclerosis patients with clinically isolated syndrome. *Magn Reson Med* **68**, 1932–1942 (2012). https://doi.org/10.1002/mrm.24194

56 Ponath, G. *et al.* Myelin phagocytosis by astrocytes after myelin damage promotes lesion pathology. *Brain* **140**, 399–413 (2017). https://doi.org/10.1093/brain/aww298

57 Ma, Q. *et al.* Blood-brain barrier-associated pericytes internalize and clear aggregated amyloid-beta42 by LRP1-dependent apolipoprotein E isoform-specific mechanism. *Mol Neurodegener* **13**, 57 (2018). https://doi.org/10.1186/s13024-018-0286-0

58 Baaklini, C. S. *et al.* Microglia promote remyelination independent of their role in clearing myelin debris. *Cell Rep* **42**, 113574 (2023). https://doi.org/10.1016/j.celrep.2023.113574

59 Zhou, T. *et al.* Microvascular endothelial cells engulf myelin debris and promote macrophage recruitment and fibrosis after neural injury. *Nat Neurosci* **22**, 421–435 (2019). https://doi.org/10.1038/s41593-018-0324-9

60 Halder, S. K. & Milner, R. Hypoxia in multiple sclerosis; is it the chicken or the egg? *Brain* **144**, 402–410 (2021). https://doi.org/10.1093/brain/awaa427

61 Mahad, D., Ziabreva, I., Lassmann, H. & Turnbull, D. Mitochondrial defects in acute multiple sclerosis lesions. *Brain* **131**, 1722–1735 (2008). https://doi.org/10.1093/brain/awn105

62 Gonul, E. *et al.* Early pericyte response to brain hypoxia in cats: an ultrastructural study. *Microvasc Res* **64**, 116–119 (2002). https://doi.org/10.1006/mvre.2002.2413

63 Liu, M. *et al.* Biglycan stimulates retinal pathological angiogenesis via up-regulation of CXCL12 expression in pericytes. *FASEB J* **39**, e70262 (2025). https://doi.org/10.1096/fj.202401903R

64 Islam, M. M. *et al.* Single-pericyte nanomechanics measured by contraction cytometry. *APL Bioeng* **8**, 036109 (2024). https://doi.org/10.1063/5.0213761

65 Yemisci, M. *et al.* Pericyte contraction induced by oxidative-nitrative stress impairs capillary reflow despite successful opening of an occluded cerebral artery. *Nat Med* **15**, 1031–1037 (2009). https://doi.org/10.1038/nm.2022

66 Berthiaume, A. A. *et al.* Dynamic Remodeling of Pericytes In Vivo Maintains Capillary Coverage in the Adult Mouse Brain. *Cell Rep* **22**, 8–16 (2018). https://doi.org/10.1016/j.celrep.2017.12.016

67 Buch, S. *et al.* Revealing vascular abnormalities and measuring small vessel density in multiple sclerosis lesions using USPIO. *Neuroimage Clin* **29**, 102525 (2021). https://doi.org/10.1016/j.nicl.2020.102525

68 Holley, J. E., Newcombe, J., Whatmore, J. L. & Gutowski, N. J. Increased blood vessel density and endothelial cell proliferation in multiple sclerosis cerebral white matter. *Neurosci Lett* **470**, 65–70 (2010). https://doi.org/10.1016/j.neulet.2009.12.059

69 Dickson, A. S. *et al.* A HIF independent oxygen-sensitive pathway for controlling cholesterol synthesis. *Nat Commun* **14**, 4816 (2023). https://doi.org/10.1038/s41467-023-40541-1

70 Sodhi, A. *et al.* Angiopoietin-like 4 binds neuropilins and cooperates with VEGF to induce diabetic macular edema. *J Clin Invest* **129**, 4593–4608 (2019). https://doi.org/10.1172/JCI120879

71 Hung, C. F. *et al.* Pericyte-like cells undergo transcriptional reprogramming and distinct functional adaptations in acute lung injury. *FASEB J* **35**, e21323 (2021). https://doi.org/10.1096/fj.201903192RR

72 Wieczorek, M. *et al.* Major Histocompatibility Complex (MHC) Class I and MHC Class II Proteins: Conformational Plasticity in Antigen Presentation. *Front Immunol* **8**, 292 (2017). https://doi.org/10.3389/fimmu.2017.00292

73 Balabanov, R., Beaumont, T. & Dore-Duffy, P. Role of central nervous system microvascular pericytes in activation of antigen-primed splenic T-lymphocytes. *Journal of Neuroscience Research* **55**, 578–587 (1999). https://doi.org/10.1002/(sici)1097-4547(19990301)55:5<578::Aid-jnr5>3.0.Co;2-e

74 Koch, K. *et al.* CNS Pericytes Modulate Local T Cell Infiltration in EAE. *Int J Mol Sci* **23** (2022). https://doi.org/10.3390/ijms232113081

75 Pardridge, W. M., Buciak, Y. J. & Tourtellotte, W. W. Human brain microvascular DR-antigen. *Journal of Neuroscience Research* **23**, 337–341 (1989). https://doi.org/10.1002/jnr.490230314

76 Smith, A. M. *et al.* Adult human glia, pericytes and meningeal fibroblasts respond similarly to IFNy but not to TGFbeta1 or M-CSF. *PLoS One* **8**, e80463 (2013). https://doi.org/10.1371/journal.pone.0080463

77 Traugott, U. & Lebon, P. Interferon-γ and Ia antigen are present on astrocytes in active chronic multiple sclerosis lesions. *Journal of the Neurological Sciences* **84**, 257–264 (1988). https://doi.org/10.1016/0022-510X(88)90130-X

78 Selmaj, K., Raine, C. S., Cannella, B. & Brosnan, C. F. Identification of lymphotoxin and tumor necrosis factor in multiple sclerosis lesions. *J Clin Invest* **87**, 949–954 (1991). https://doi.org/10.1172/JCI115102

79 Jakimovski, D. *et al.* Lower arterial cerebral blood flow is associated with worse neuroinflammation and immunomodulation composite proteomic scores. *Mult Scler Relat Disord* **87**, 105687 (2024). https://doi.org/10.1016/j.msard.2024.105687

80 Jakimovski, D. *et al.* Lower cerebral arterial blood flow is associated with greater serum neurofilament light chain levels in multiple sclerosis patients. *Eur J Neurol* **29**, 2299–2308 (2022). https://doi.org/10.1111/ene.15374

81 Doi, T., Sugimoto, H., Arimoto, I., Hiroaki, Y. & Fujiyoshi, Y. Interactions of endothelin receptor subtypes A and B with Gi, Go, and Gq in reconstituted phospholipid vesicles. *Biochemistry* **38**, 3090–3099 (1999). https://doi.org/10.1021/bi981919m

82 Berthiaume, A. A. *et al.* Pericyte remodeling is deficient in the aged brain and contributes to impaired capillary flow and structure. *Nat Commun* **13**, 5912 (2022). https://doi.org/10.1038/s41467-022-33464-w

83 Nikolakopoulou, A. M. *et al.* Pericyte loss leads to circulatory failure and pleiotrophin depletion causing neuron loss. *Nat Neurosci* **22**, 1089–1098 (2019). https://doi.org/10.1038/s41593-019-0434-z

84 Andueza, A. *et al.* Endothelial Reprogramming by Disturbed Flow Revealed by Single-Cell RNA and Chromatin Accessibility Study. *Cell Rep* **33**, 108491 (2020). https://doi.org/10.1016/j.celrep.2020.108491

85 Cruz Hernandez, J. C. *et al.* Neutrophil adhesion in brain capillaries reduces cortical blood flow and impairs memory function in Alzheimer's disease mouse models. *Nat Neurosci* **22**, 413–420 (2019). https://doi.org/10.1038/s41593-018-0329-4

86 Coelho-Santos, V., Berthiaume, A. A., Ornelas, S., Stuhlmann, H. & Shih, A. Y. Imaging the construction of capillary networks in the neonatal mouse brain. *Proc Natl Acad Sci U S A* **118** (2021). https://doi.org/10.1073/pnas.2100866118

87 Gaitan, M. I., de Alwis, M. P., Sati, P., Nair, G. & Reich, D. S. Multiple sclerosis shrinks intralesional and enlarges extralesional brain parenchymal veins. *Neurology* **80**, 145–151 (2013). https://doi.org/10.1212/WNL.0b013e31827b916f

88 Sisco, N. J., Borazanci, A., Dortch, R. & Stokes, A. M. Investigating the relationship between multi-scale perfusion and white matter microstructural integrity in patients with relapsing-remitting MS. *Mult Scler J Exp Transl Clin* **7**, 20552173211037002 (2021). https://doi.org/10.1177/20552173211037002

89 Mujanovic, A. *et al.* No-reflow phenomenon in stroke patients: A systematic literature review and meta-analysis of clinical data. *Int J Stroke* **19**, 58–67 (2024). https://doi.org/10.1177/17474930231180434

90 Desai, R. A. *et al.* Nimodipine Reduces Dysfunction and Demyelination in Models of Multiple Sclerosis. *Ann Neurol* **88**, 123–136 (2020). https://doi.org/10.1002/ana.25749

91 Korte, N. *et al.* Inhibiting Ca(2+) channels in Alzheimer's disease model mice relaxes pericytes, improves cerebral blood flow and reduces immune cell stalling and hypoxia. *Nat Neurosci* **27**, 2086–2100 (2024). https://doi.org/10.1038/s41593-024-01753-w

92 Patel, H. *et al.* nf-core/rnaseq: nf-core/rnaseq v3.12.0 - Osmium Octopus (3.12.0). *Zenodo* (2023). https://doi.org/10.5281/zenodo.7998767

93 Krueger, F. *et al.* TrimGalore: v0.6.10. *Zenodo* (2023). https://doi.org/10.5281/zenodo.7598955

94 Love, M. I., Huber, W. & Anders, S. Moderated estimation of fold change and dispersion for RNA-seq data with DESeq2. *Genome Biology* **15** (2014). https://doi.org/10.1186/s13059-014-0550-8

95 Soneson, C., Love, M. I. & Robinson, M. D. Differential analyses for RNA-seq: transcript-level estimates improve gene-level inferences. *F1000Research* **4**, 1521 (2015). https://doi.org/10.12688/f1000research.7563.1

96 Risso, D., Ngai, J., Speed, T. P. & Dudoit, S. Normalization of RNA-seq data using factor analysis of control genes or samples. *Nature Biotechnology* **32**, 896–902 (2014). https://doi.org/10.1038/nbt.2931

97 Blighe, L., Rana, S. & Lewis, M. EnhancedVolcano: Publication-ready volcano plots with enhanced colouring and labeling. (2018).

98 Kolde, R. Pheatmap: pretty heatmaps. (2012).

99 Wickham, H. *ggplot2: Elegant Graphics for Data Analysis.*, (Springer-Verlag, 2016).

100 Vitting-Seerup, K. & Sandelin, A. IsoformSwitchAnalyzeR: analysis of changes in genome-wide patterns of alternative splicing and its functional consequences. *Bioinformatics* **35**, 4469–4471 (2019). https://doi.org/10.1093/bioinformatics/btz247

101 Anders, S., Reyes, A. & Huber, W. Detecting differential usage of exons from RNA-seq data. *Genome Res* **22**, 2008–2017 (2012). https://doi.org/10.1101/gr.133744.111

102 Wu, T. *et al.* clusterProfiler 4.0: A universal enrichment tool for interpreting omics data. *The Innovation* **2**, 100141 (2021). https://doi.org/10.1016/j.xinn.2021.100141

103 Badia-i-Mompel, P. *et al.* decoupleR: ensemble of computational methods to infer biological activities from omics data. *Bioinformatics Advances* **2**, 1–3 (2022). https://doi.org/10.1093/bioadv/vbac016

104 King, N. E. *et al.* Pharmacological PDGFRbeta inhibitors imatinib and sunitinib cause human brain pericyte death in vitro. *Toxicol Appl Pharmacol* **444**, 116025 (2022). https://doi.org/10.1016/j.taap.2022.116025

105 Bankhead, P. *et al.* QuPath: Open source software for digital pathology image analysis. *Sci Rep* **7**, 16878 (2017). https://doi.org/10.1038/s41598-017-17204-5

106 Rolfe, A. J., Bosco, D. B., Broussard, E. N. & Ren, Y. In Vitro Phagocytosis of Myelin Debris by Bone Marrow-Derived Macrophages. *J Vis Exp* (2017). https://doi.org/10.3791/56322

hPSC$^{reg®}$ Line	Group	Sex	Age at Collection
MNZTASi009-A	Control	F	
MNZTASi019-A	Control	F	
MNZTASi020-A	Control	F	
MNZTASi021-A	Control	M	
MNZTASi022-A	Control	F	
MNZTASi024-A	Control	F	
MNZTASi032-A	Control	M	
MNZTASi040-A	Control	M	
MNZTASi050-A	Control	M	
MNZTASi070-A	Control	M	
MNZTASi002-A	Family RoMS	F	
MNZTASi003-A	Family RoMS	F	
MNZTASi004-A	Family RoMS	F	
MNZTASi005-A	Family RoMS	M	
MNZTASi007-A	RoMS	F	
MNZTASi010-A	RoMS	F	
MNZTASi014-A	RoMS	F	
MNZTASi016-A	RoMS	F	
MNZTASi017-A	RoMS	F	
MNZTASi018-A	RoMS	F	
MNZTASi033-A	RoMS	M	
MNZTASi037-A	RoMS	M	

1052 **Table 1: iPSC line details and disease status**

1053

Figures

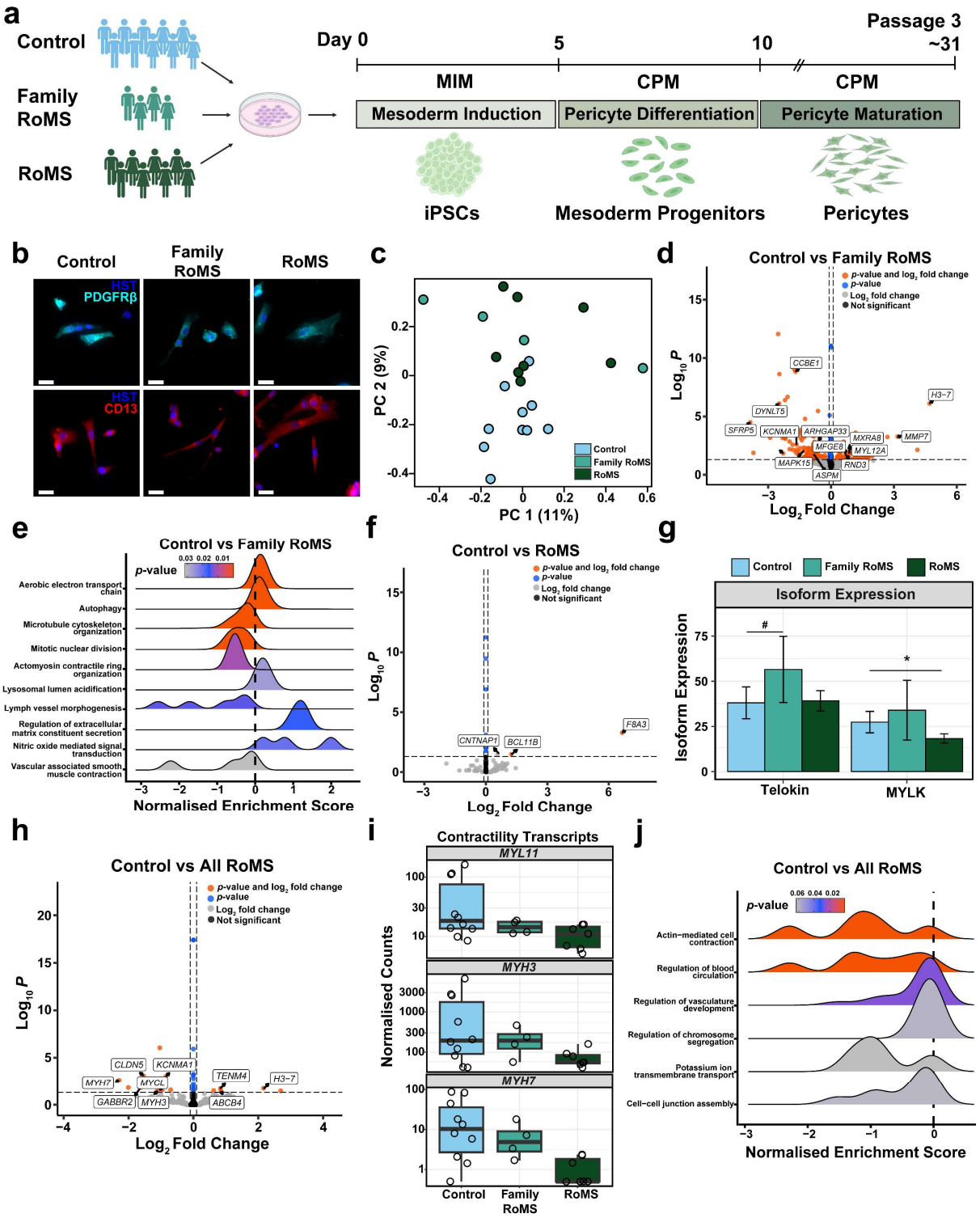

Figure 1: Gene expression differs between iPericytes from people with or without RoMS (a) Experimental design and timeline of pericyte differentiation. (b) Images (20x) of PDGFRβ (cyan) and CD13 (red) expression by iPericytes. Scale bars, 50μm. (c) Principal component analysis of gene expression incorporating 1 factor of

1061 unwanted variation (n=10 Control, n=4 Family RoMS and n=8 RoMS cell lines). (d)
1062 Volcano plot showing genes that are differentially expressed between Control (n=10
1063 lines) and Family RoMS (n=4 lines) iPericytes. Adjusted p-value <0.05 and Log2 fold
1064 change ≥0.1. (e) Ridge plot showing gene set enrichment analysis results comparing
1065 Control and Family RoMS iPericytes. (f) Volcano plot showing genes that are
1066 differentially expressed between Control (n=10 lines) and RoMS (n=8 lines) iPericytes.
1067 (g) Barplots showing the isoform expression for *MYLK*. Data expressed as mean ±
1068 standard deviation for n=10 Control or n=4 Family RoMS or n=8 RoMS iPericyte
1069 cultures. (h) Volcano plot showing genes that are differentially expressed between
1070 Control (n=10 lines) and Family RoMS (n=4 lines) combined with RoMS (n=8 lines)
1071 iPericytes. (i) Boxplots showing gene expression in Control, Family RoMS and RoMS
1072 iPericytes, for DEGs with known biological roles that may impact pericyte contractility.
1073 Data expressed as median ± interquartile range. Dot points represent individual
1074 cultures from n=10 Control or n=4 Family RoMS or n=8 RoMS iPericyte cultures. (j)
1075 Ridge plot showing gene set enrichment analysis results comparing Control and all
1076 RoMS iPericytes. False discovery rate adjustment was used for multiple testing for
1077 RNAseq data.

1078

1079

1080

1081

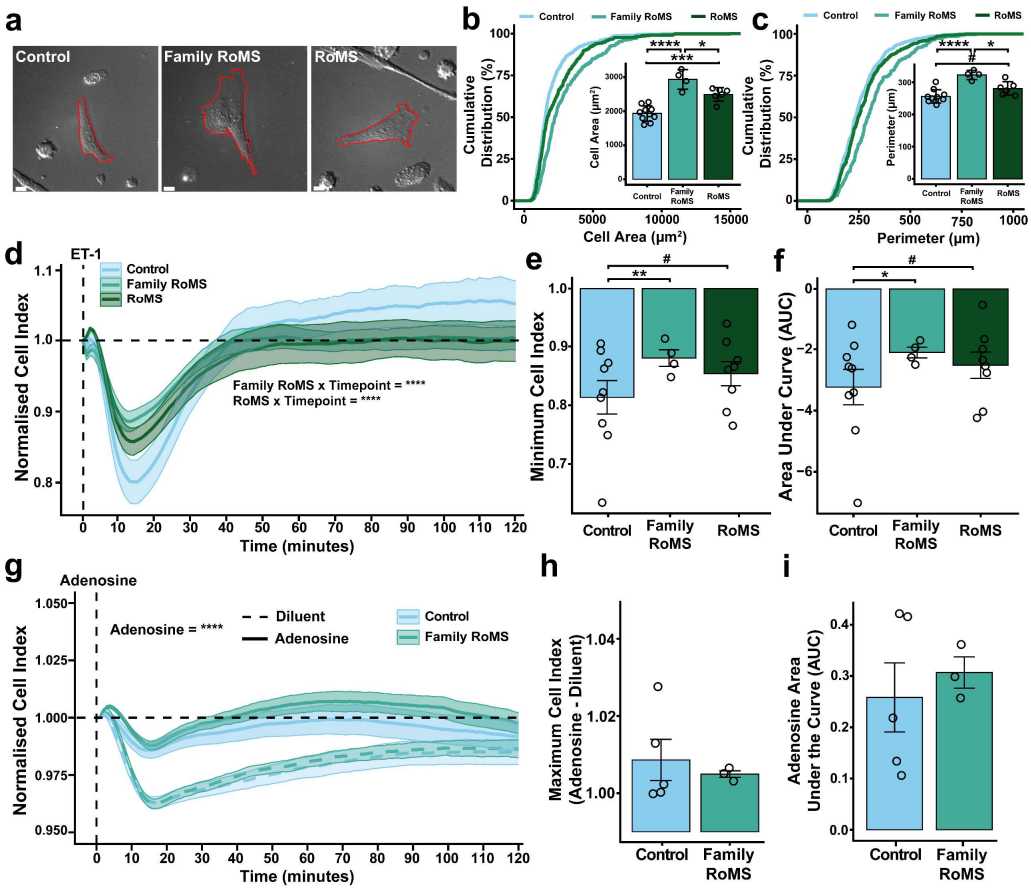

Figure 2: Enlarged RoMS iPericytes have a reduced contractile response to endothelin-1 (ET-1). (a) Images of Control, Family RoMS and RoMS pericytes with their perimeter traced for morphological assessment (red). Scale bars, 10µm. (b) Cumulative distribution plot of iPericyte cell area. > 50 cells evaluated per cell line for n=10 Control, n=4 Family RoMS and n=8 RoMS lines. Inset graph depicts the mean cell area per group ± standard deviation, and dots represent the mean for individual cell lines. (c) Cumulative distribution plot of iPericyte perimeter. > 50 cells evaluated in each of n=10 Control, n=4 Family RoMS and n=8 RoMS lines. Inset graph depicts the mean cell perimeter per group ± standard deviation. (d) Normalised electrical impedance cell index for Control, Family RoMS and RoMS iPericytes responding to ET-1 over a 2 hour period. 2-4 wells evaluated per cell line to obtain the average per cell line. Data presented represent the group mean ± SEM for n=9 Control, n=4 Family RoMS and n=8 RoMS cell lines. (e,f) Quantification of the minimum cell index (maximum pericyte contraction) or area under the curve for the first 20 minutes following ET-1 treatment of Control, Family RoMS and RoMS iPericytes. 2-4 wells were evaluated to obtain the average for each cell line and data are presented as mean for each group ± SEM from n=9 Control, n=4 Family RoMS and n=8 RoMS lines. (g) Normalised electrical impedance cell index for Control and Family RoMS iPericytes following adenosine exposure. 2-4 wells were evaluated to obtain a per cell line average. Data are presented as mean per group ± SEM for n=5 Control or n=3 Family RoMS lines. (h) Quantification of the maximum cell index (level of relaxation) for Control and Family RoMS iPericytes exposed to diluent or adenosine. 2-4 wells were evaluated to obtain a per cell line average. Data presented represent the mean per

1106 treatment ± SEM for n=5 Control and n=3 Family RoMS lines. (i) Area under the curve
1107 for the first 20 minutes following adenosine treatment of Control or Family RoMS
1108 iPericytes. Data presented represent the mean per treatment ± SEM for n=5 Control
1109 and n=3 Family RoMS lines. #<0.1, ∗p<0.05, ∗∗p<0.01 ∗∗∗p<0.001, ∗∗∗∗p<0.0001.
1110 Restricted maximum likelihood linear mixed model with pairwise comparisons using
1111 Tukey's adjustment for p-values.

1112

1113

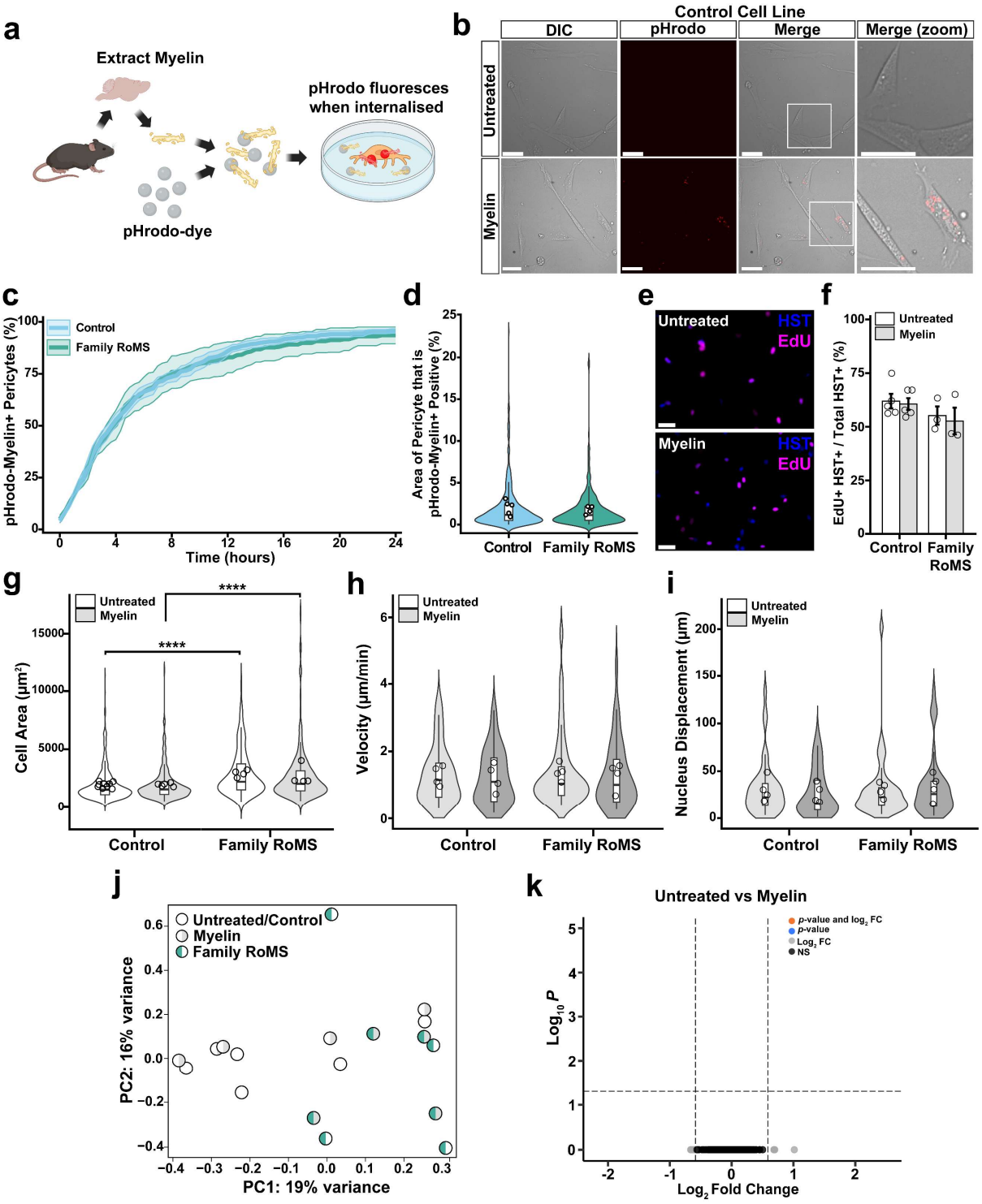

Figure 3: iPericytes phagocytose myelin debris but this is not associated with morphologically or transcriptional changes. (a) Schematic of mouse myelin extraction and the treatment of iPericytes. (b) Epifluorescence and phase contrast images (20x) of iPericytes cultured without (untreated) or with pHrodo-tagged myelin debris for 20 hours. Scale bars, 50µm. (c) Quantification of the percentage (%) of Control or Family RoMS iPericytes that phagocytosed myelin and became pHrodo^{+} over time (imaged every 20 minutes for 20 hours). > 50 cells evaluated per cell line; n=5 Control and n=4 Family RoMS cell lines. Data expressed as mean per group ±

SEM. (d) Quantification of iPericytes area with myelin-pHrodo^{+} pixels (%) was calculated for n=5 Control and n=4 Family RoMS lines (> 100 cells evaluated per line). Data expressed as median ± interquartile range, dots represent cell line mean. (e) Images (10x) of iPericytes that incorporated EdU (red) under untreated or myelin conditions. Scale bars, 50µm. (f) The percentage (%) of iPericytes per culture that became EdU+ over 20 hours in untreated and myelin conditions. 4-9 wells were evaluated per n=5 Control and n=3 Family RoMS lines. Data are expressed as mean ± SEM, where individual dots represent the mean for each cell line. (g) Quantification of iPericyte cell area. > 50 cells were measured per line per treatment condition for n=5 Control and n=4 Family RoMS lines. Data are expressed as median ± interquartile range, and individual dots represent the cell line means. (h) Quantification of the mean velocity of iPericytes under untreated and myelin conditions. Velocity was determined for > 10 cells per line per treatment. Data are expressed as median ± interquartile range, and individual dots represent cell line means. (i) Quantification of nucleus displacement between t=0 and t=60 minutes of imaging for iPericytes under untreated or myelin conditions. Displacement was measured for > 10 cells per line per treatment for n=4 Control and n=4 Family RoMS lines. Data are expressed as median ± interquartile range, and individual dot points represent cell line means. (j) Principal component analysis of gene expression in untreated or myelin treated iPericytes. (k) Volcano plot comparing gene expression in iPericytes cultured without or with myelin debris. Adjusted *p*-value <0.05 and Log2 fold change ≥ 0.585; n=9 (n=5 Control and n=4 Family RoMS) lines. Restricted maximum likelihood linear mixed model with pairwise comparisons using Tukey's adjustment for p-values. False discovery rate adjustment was used for multiple testing for RNAseq data. ****p<0.0001.

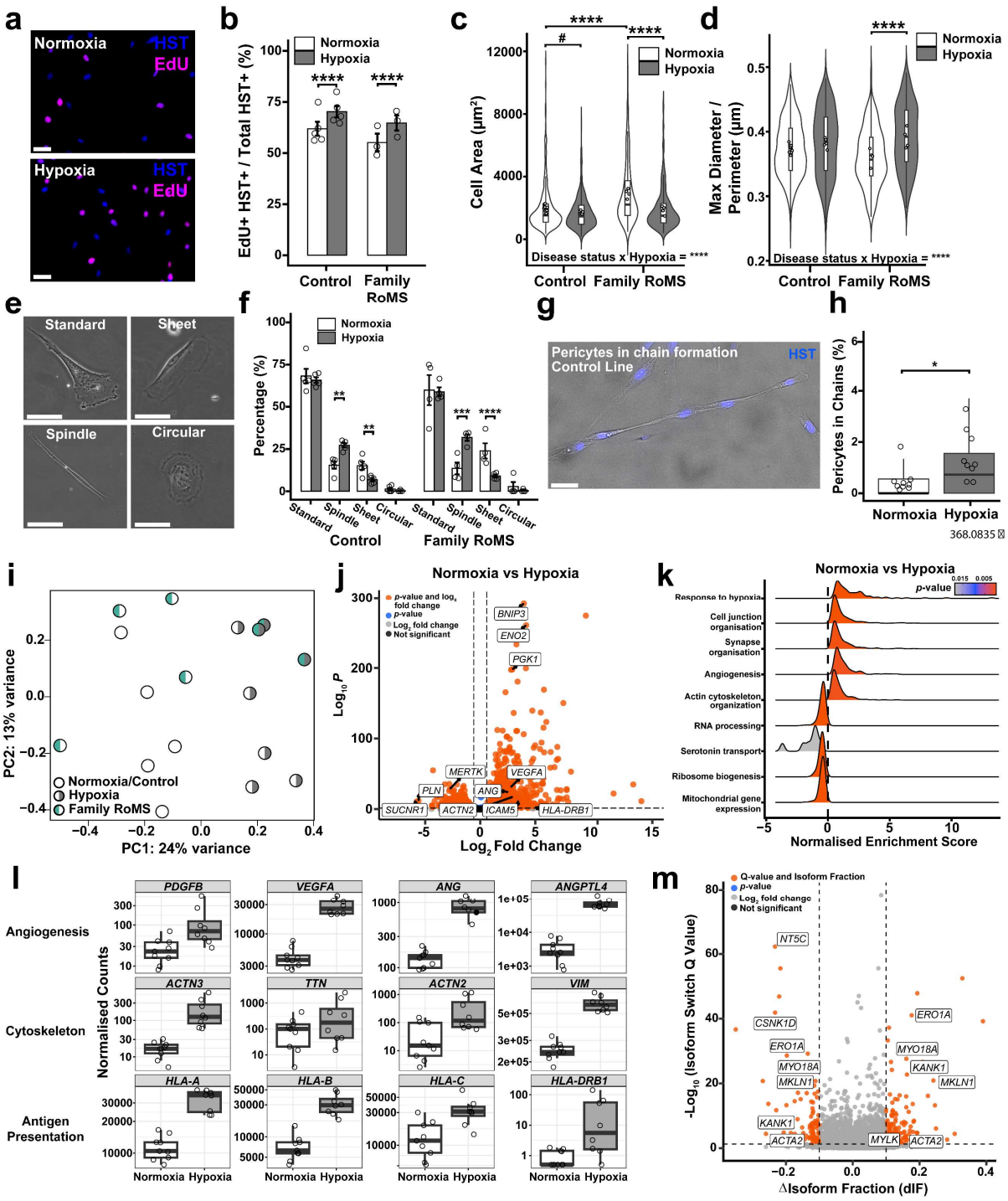

Figure 4: Hypoxia induces proliferation and alters the morphology and transcriptomic profile of iPericytes. (a) Images (10x) of Control iPericytes that incorporate EdU (magenta) when cultured under normoxic or hypoxic (0.5% O_2) conditions for 20 hours. Scale bars, 50µm. (b) Quantification of the percentage of cells in Control or Family RoMS iPericyte cultures that were EdU^+ after 20 hours of exposure to a normoxic or hypoxic environment. 4-9 wells analysed per line per treatment for n=5 Control and n=3 Family RoMS lines. Data are expressed as mean ± SEM, and individual dots represent cell line means. (c,d) Quantification of iPericyte cell area or max Feret diameter (max diameter/perimeter) for Control and Family RoMS iPericytes

grown under normoxic or hypoxic conditions. > 50 cells measured per cell line per treatment for n=10 Control and n=4 Family RoMS lines. Data are expressed as median ± interquartile range, and individual dot points represent cell line means. (e) Images (20x) showing example Control iPericyte morphologies: standard, spindle, sheet and circular. Scale bars, 50 µm. (f) Quantification of the percentage (%) of iPSC pericytes in Control or Family RoMS cultures that adopted each morphological subtype when cultured under normoxic or hypoxic conditions. > 22 cells were measured per line per treatment for n=5 Control and n=4 Family RoMS lines. Data are expressed as mean ± SEM, individual dot points represent cell line means and was analysed using a binomial generalised linear mixed model. (g) Image (10x) of Hoechst^{+} Control iPericytes cultured under hypoxic conditions, forming a chain. Scale bar, 50µm. (h) Quantification of the percentage (%) of iPericytes forming chains under normoxic and hypoxic conditions. 4-9 wells analysed per line per treatment for n=9 (n=5 Control, n=4 Family RoMS) lines. Data for Control and Family RoMS lines were combined as the response was equivalent. Data are expressed as median ± interquartile range, and individual dot points represent cell line means. (i) Principal component analysis of gene expression in iPericytes cultured under normoxic or hypoxic conditions (n=5 Control, n=3-4 Family RoMS cell lines per treatment condition). (j) Volcano plot showing genes that are differentially expressed between iPericytes cultured under normoxic or hypoxic conditions. Adjusted p-value <0.05 and Log2 fold change ≥0.585; data from n=8 (n=5 Control and n=3-4 Family RoMS) lines were combined as MS status did not impact response to hypoxia. (k) Ridge plot showing gene set enrichment analysis results comparing normoxic and hypoxic iPericytes. (l) Boxplots showing gene expression in normoxic and hypoxic iPSC pericytes, for differentially expressed genes associated with angiogenesis, cytoskeletal regulation and antigen presentation. Data are expressed as median ± interquartile range, and individual dot points represent cell line means (n=5 Control and n=3-4 Family RoMS per treatment condition). (m) Volcano plot showing genes that have isoform switches between iPericytes cultured under normoxic or hypoxic conditions (n=5 Control and n=3-4 Family RoMS per treatment condition). Restricted maximum likelihood linear mixed model with pairwise comparisons using Tukey's adjustment for p-values. #<0.1, ∗p<0.05, ∗∗p<0.01, ∗∗∗∗p<0.0001. False discovery rate adjustment was used for multiple testing for RNAseq data.

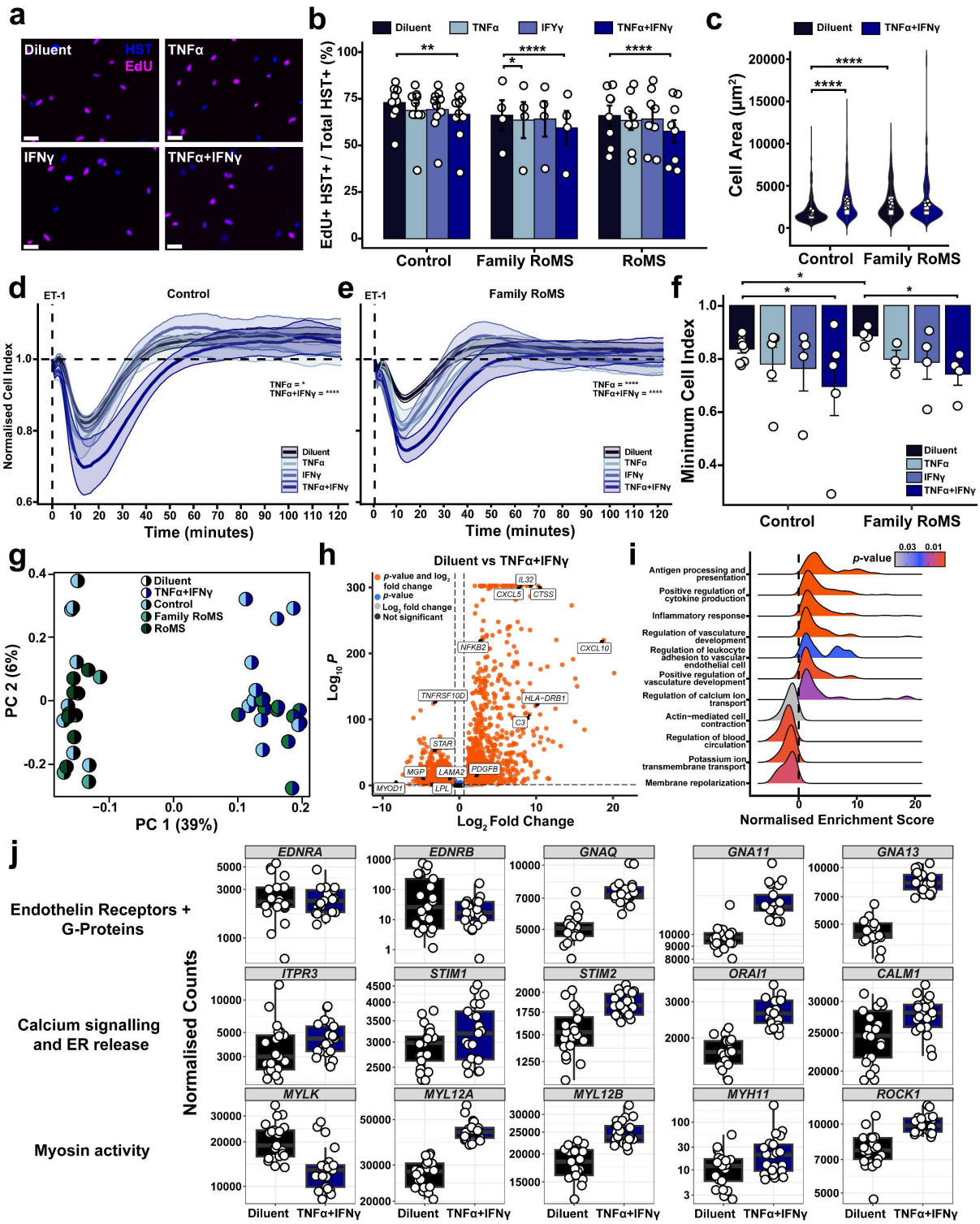

Figure 5: MS-associated inflammatory cytokines reduce proliferation, increase cell size and enhance contractility of iPericytes. (a) Images (10x) of EdU⁺ (magenta) Control iPericytes following 20 hours of diluent, TNFα, IFNγ or TNFα+IFNγ treatment. Scale bars, 50μm. (b) Quantification of the percentage (%) of cells within Control, Family RoMS and RoMS iPericyte cultures that incorporated EdU when cultured with diluent, TNFα, IFNγ or TNFα+IFNγ for 20 hours. 4-9 wells were analysed per line per treatment for n=10 Control, n=4 Family RoMS and n=8 RoMS cell lines.

Data are expressed as mean ± SEM, and individual dot points represent cell line means. (c) Quantification of Control, Family RoMS and RoMS iPericyte area for cells cultured with diluent or TNFα+IFNγ. >50 cells were measured per line per treatment for n=10 Control and n=4 Family RoMS lines. Data are expressed as median ± interquartile range, and individual dot points represent line mean. (d,e) Normalised electrical impedance cell index of Control and Family RoMS iPericytes cultured with diluent, TNFα, IFNγ or TNFα+IFNγ for 20 hours prior to exposure to ET-1. Data are normalised to cell index at the time of endothelin-1 addition. 2-7 wells were analysed per cell line for n=5-10 Control and n=3-4 Family RoMS lines. Data are expressed as mean ± SEM. (f) The normalised minimum cell index (maximum contraction) after treating Control or Family RoMS iPericytes with diluent, TNFα, IFNγ or TNFα+IFNγ. 2-7 wells were evaluated per cell line for n=5-10 Control and n=3-4 Family RoMS lines. (g) Principal component analysis of gene expression in iPericytes cultured with diluent or TNFα+IFNγ treatment (n=10 Control, n=4 Family RoMS and n=8 RoMS cell lines per treatment condition). (h) Volcano plot showing genes that are differentially expressed between iPericytes cultured with diluent or TNFα+IFNγ treatment. Adjusted p-value <0.05 and Log2 fold change ≥0.585; data from n=22 (n=10 Control and n=4 Family RoMS and n=8 RoMS) lines were combined as MS status did not impact response to TNFα+IFNγ. (i) Ridge plot showing gene set enrichment analysis results comparing diluent and TNFα+IFNγ treated iPericytes. (j) Boxplots showing gene expression from diluent and TNFα+IFNγ treated iPericytes, for differentially expressed genes associated with endothelin receptors, calcium signalling and myosin activity. Data are expressed as median ± interquartile range, and individual dot points represent cell line means (n=10 Control, n=4 Family RoMS and n=8 RoMS cell lines per treatment condition). Data are expressed as mean ± SEM. Restricted maximum likelihood linear mixed model with pairwise comparisons using Tukey's adjustment for p-values. $*p<0.05$, $**p<0.01$, $****p<0.0001$. False discovery rate adjustment was used for multiple testing for RNAseq data

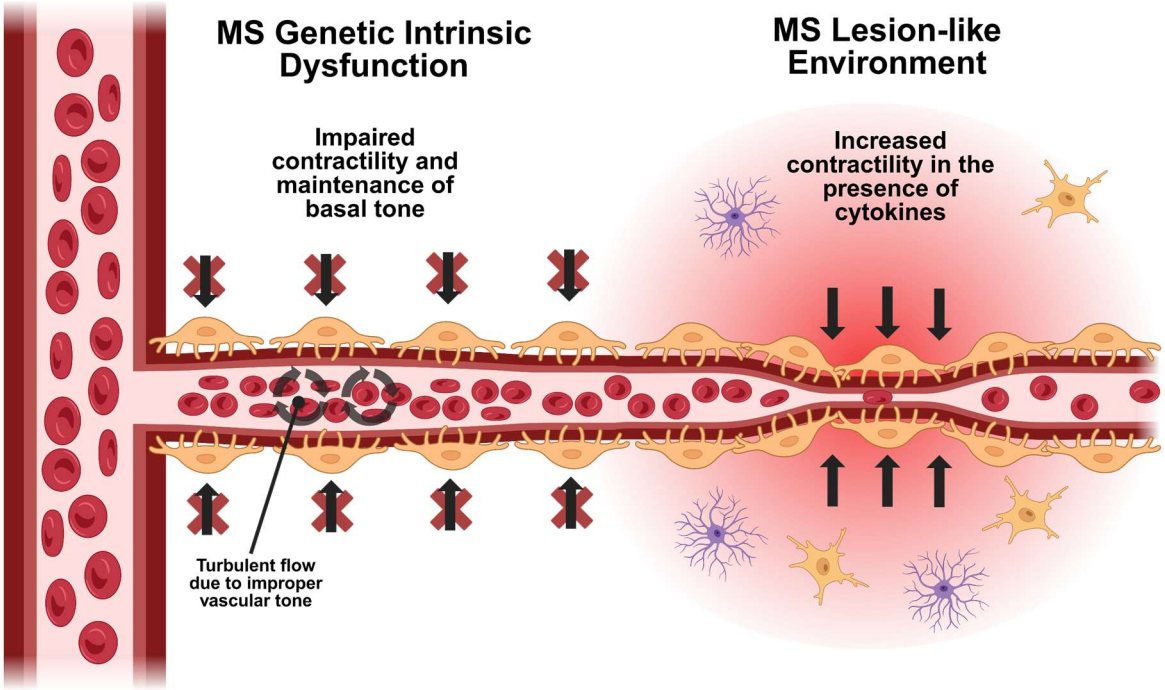

1229
1230 **Figure 6: Pericyte dysfunction in multiple sclerosis**

1231 Schematic illustrating how intrinsic pericyte dysfunction and heightened contractile
1232 responses to an MS lesion–like inflammatory environment converge to disrupt
1233 vascular tone and impair cerebral capillary blood flow.

1234